EUROPEAN ORGANIZATION FOR NUCLEAR RESEARCH

JET PRODUCTION AND FRAGMENTATION PROPERTIES IN DEEP INELASTIC MUON SCATTERING

CERN-EP/87-112
June 24th, 1987

The European Muon Collaboration

Aachen[1], CERN[2], DESY (Hamburg)[3], Freiburg[4], Hamburg (University)[5],
Kiel[6], LAL (Orsay)[7], Lancaster[8], LAPP (Annecy)[9], Liverpool[10], Marseille[11],
Mons[12], MPI (München)[13], Oxford[14], RAL (Chilton)[15], Sheffield[16],
Torino[17], Uppsala[18], Warsaw[19], Wuppertal[20].

M. Arneodo[17], A. Arvidson[18], J.J. Aubert[11], B. Badelek[19a)],
J. Beaufays[2], C.P. Bee[8b)], C. Benchouk[11], G. Berghoff[1], I. Bird[8c)],
D. Blum[7], E. Böhm[6], X. de Bouard[9], F.W. Brasse[3], H. Braun[20],
C. Broll[9+)], S. Brown[10d)], H. Brück[20e)], H. Calen[18], J.S. Chima[15f)],
J. Ciborowski[19a], R. Clifft[15], G. Coignet[9], F. Combley[16], J. Conrad[14],
J. Coughlan[8g)], G. D'Agostini[11], S. Dahlgren[18], F. Dengler[13],
I. Derado[13], T. Dreyer[4], J. Drees[20], M. Drobnitzki[1], M. Düren[1],
V. Eckardt[13], A. Edwards[20h)], M. Edwards[15], T. Ernst[4], G. Eszes[9i)],
J. Favier[9], M.I. Ferrero[17], J. Figiel[5j)], W. Flauger[3], J. Foster[16k)],
J. Ftàčnik[13], E. Gabathuler[10], J. Gajewski[5], R. Gamet[10], J. Gayler[3],
N. Geddes[14g)], P. Grafström[18l)], F. Grard[12], J. Haas[4], E. Hagberg[18],
F.J. Hasert[1m)], P. Hayman[10], P. Heusse[7], M. Jaffré[7], A. Jacholkowska[2],
F. Janata[5], G. Jancso[13i)], A.S. Johnson[14n)], E.M. Kabuss[4],
G. Kellner[2], V. Korbel[3], A. Krüger[5], J. Krüger[20e)], S. Kullander[18],
U. Landgraf[4], D. Lanske[1], J. Loken[14], K. Long[14l)], M. Maire[9],
P. Malecki[13], A. Manz[13], S. Maselli[17o)], W. Mohr[4], F. Montanet[11],
H.E. Montgomery[2p)], E. Nagy[9i)], J. Nassalski[19q)], P.R. Norton[15],
F.G. Oakham[15r)], A.M. Osborne[2], C. Pascaud[7], B. Pawlik[13], P. Payre[11],
C. Peroni[17], H. Peschel[20], H. Pessard[9], J. Pettingale[10], B. Pietrzyk[11],
U. Pietrzyk[20], B. Pönsgen[5], M. Pötsch[20], P. Renton[14], P. Ribarics[9i)],
K. Rith[4c)], E. Rondio[19], A. Sandacz[19q)], M. Scheer[1], A. Schlagböhmer[4],
H. Schiemann[5], N. Schmitz[13], M. Schneegans[9], M. Scholz[1], T. Schröder[4],
K. Schultze[1], T. Sloan[8], H.E. Stier[4], M. Studt[5], G.N. Taylor[14s)],
J.M. Thénard[9], J.C. Thompson[15], A. de la Torre[5t)], J. Toth[9i)],
L. Urban[1], L. Urban[9i)], W. Wallucks[4], M. Whalley[16u)],
S. Wheeler[16], W.S.C. Williams[14], S.J. Wimpenny[10p)],
R. Windmolders[12], G. Wolf[13], K. Ziemons[1]

(Submitted to Zeitschrift für Physik C)

ABSTRACT

Results are presented from a study of deep inelastic 280 GeV muon-nucleon interactions on the transverse momenta and jet properties of the final state hadrons. The results are analysed in a way which attempts to separate the contributions of hard and soft QCD effects from those that arise from the fragmentation process. The fragmentation models with which the data are compared are the Lund string model, the independent jet model, the QCD parton shower model including soft gluon interference effects, and the firestring model. The discrimination between these models is discussed. Various methods of analysis of the data in terms of hard QCD processes are presented. From a study of the properties of the jet profiles a value of α_s, to leading order, is determined using the Lund string model, namely α_s=0.29±0.01 (stat.) ±0.02 (syst.), for Q^2~20 GeV^2.

For footnotes see next page

Addresses

1) III. Physikalisches Inst. A, Physikzentrum, Aachen, Germany.
2) CERN, Geneva, Switzerland.
3) DESY, Hamburg, Germany.
4) Fakultät für Physik, Universität Freiburg, Germany.
5) II Institut für Experimentalphysik, Universität Hamburg, Germany.
6) II Institut für Kernphysik, Universität Kiel, Germany.
7) Laboratoire de l'Accélérateur Linéaire, Université de Paris-Sud, Orsay, France.
8) Department of Physics, University of Lancaster, England.
9) Laboratoire d'Annecy de Physique des Particles, IN2P3, Annecy-le-Vieux, France.
10) Department of Physics, University of Liverpool, England.
11) Centre de Physique des Particules, Faculté des Sciences de Luminy, Marseille, France.
12) Faculté des Sciences, Université de L'Etat à Mons, Belgium.
13) Max-Planck-Institut für Physik und Astrophysik, München, Germany.
14) Nuclear Physics Laboratory, University of Oxford, England.
15) Rutherford and Appleton Laboratory, Chilton, Didcot, England.
16) Department of Physics, University of Sheffield, England.
17) Istituto di Fisica, Università di Torino, Italy.
18) Gustav Werners Institut, University of Uppsala, Sweden.
19) Physics Institute, University of Warsaw, and
Institute for Nuclear Studies, Warsaw, Poland.
20) Fachbereich Physik, Universität Wuppertal, Germany.

a) University of Warsaw, Poland.
b) Now at University of Liverpool, England.
c) Now at MPI für Kernphysik, Heidelberg, Germany.
d) Now at TESA S.A., Renens, Switzerland.
e) Now at DESY, Hamburg, W. Germany.
f) Now at British Telecom, PLC, Ipswich, England.
g) Now at RAL, Chilton, Didcot, England.
h) Now at Jet, Joint Undertaking, Abingdon, England.
i) Permanent address: Central Research Institute for Physics of the Hungarian Academy of Science, Budapest, Hungary.
j) Now at Institute of Nuclear Physics, Krakow, Poland.
k) Now at University of Manchester, England.
l) Now at CERN, Geneva, Switzerland.
m) Now at Krupp Atlas Elektronic GmbH, Bremen, Germany.
n) Now at SLAC, Stanford, California.
o) Now at MPI, Munich, Germany.
p) Now at FNAL, Batavia, Illinois, U.S.A.
q) Institute for Nuclear Studies, Warsaw, Poland.
r) Now at NRC, Ottawa, Canada.
s) Now at University of Melbourne, Parkville, Australia.
t) Now at Universidad Nacional, Mar del Plata, Argentina.
u) Now at University of Durham, England.
+) Deceased.

1. INTRODUCTION

The study of hadronic jets in both deep inelastic lepton-nucleon scattering and e^+e^- annihilation, has been a test bed for models of hadronic structure (principally the quark-parton model, QPM, with modifications from quantum chromodynamics, QCD) and for models describing the fragmentation of excited parton systems into final state hadrons. The discovery of the two-jet dominance in hadron production followed, at higher energies, by clearly discernable three-jet structures in e^+e^- interactions [1], led to the more detailed study of jet production in both e^+e^- and ℓ-N scattering. In this paper we describe the analysis of hadronic jet production and fragmentation in a high precision μ-N scattering experiment.

The μ-N interaction (fig. 1a) is described in terms of the Bjorken scaling variables $x_{Bj}=Q^2/(2p.q)=Q^2/(2M\nu)$ and $y=\nu/E_\mu$, where $q^2=-Q^2$ is the four-momentum transfer squared, ν is the exchanged virtual photon energy in the target nucleon rest system, E_μ is the incident muon energy and M the nucleon mass. The properties of the final state hadrons depend, in general, on y, x_{Bj} and Q^2. The energy (W) of the outgoing hadrons in their centre-of-mass system (cms), is given by $W^2=M^2+Q^2(1/x_{Bj}-1)$. Hadron properties are measured by the longitudinal variables $x_F=2p_{\parallel}/W$ (where $p_{\parallel}$ is the cms momentum component along the virtual photon, that is the current direction) or cms rapidity y* (defined as $y^*=0.5\ \ln((E+p_{\parallel})/(E-p_{\parallel}))$, where E is the cms energy of the hadron), and by the momentum component transverse to the current direction, p_T. Although the basic interaction is between the exchanged highly space-like virtual photon and one of the nucleon's parton constituents, experimentally only the hadron fragments of the excited parton state are observed. The consequence is a considerable complication in discerning between the scattering and fragmentation processes when analysing the final state hadrons.

The QPM, with the addition of processes involving gluons in QCD (fig. 1b), is a well defined prescription for calculating cross sections of high momentum transfer interactions. The processes shown in fig. 1b will, at high enough energy, lead to final states containing three distinct jets, associated with the q,g (or $q,\bar{q}$) and with the remnant target system. The low energy (long distance) development of quark and gluons into hadrons is, however, beyond reliable calculation at present. The hadronisation of the initial partons must thus be simulated with phenomenological models. This method gives information on both the parton interactions and the fragmentation process in a somewhat coupled manner. The main emphasis in the analysis is to search for effects that are more strongly dependent on one or the other. Consistency over a variety of such effects can then be imposed to decouple the two processes.

The hadronisation models used in the analysis of the present data fall into several categories. The independent-jet (IJ) models of Hoyer et al. [2] and Ali et al. [3] are based on the earlier work of Field and Feynman [4]. These prescriptions were developed mainly for experiments at electron-positron colliders and describe the development of the individual quark-antiquark pairs produced in e^+e^- interactions into final state hadrons. They both include the effects of heavy quark production as well as QCD matrix elements and gluon jets. The differences between the two models lie in the techniques used to conserve momentum, a problem due to the assumption of the independence of the jets, and the treatment of the gluon jet fragmentation. (See [2], [3] and [5] for more details).

The so called "string models" follow a different approach. Primarily developed by the Lund group [6], the string model assumes that the fragmentation occurs along the colour flux tubes which connect the coloured partons. QCD effects are included with gluons corresponding to energy and momentum carrying "kinks" on the strings. The main differences between the IJ models and the string models are manifest, for example, in events with gluon bremsstrahlung. Here the fragmentation occurs preferentially along the strings stretched between the gluon and the other partons. This string effect is evidently not present in the IJ models. Also the string provides a natural mechanism for 'cross-talk' between the fragmentation in the forward and backward hemispheres.

Models based upon "parton showers" calculated according to leading logarithm approximations have been pursued by Fox and Wolfram [7], Field and Wolfram [8] and Gottschalk [9]. They have been primarily developed for e^+e^- annihilation. The initial quark and antiquark are assumed to be far off the mass shell and evolve by successive branching into cascades of partons close to the mass shell (extending down to the cut-off, Q_o). These cascades are finally combined into colour singlet clusters of quark-antiquark pairs which decay into final state hadrons. If the cluster mass is higher than a cut-off value, Q_h, it is split into smaller clusters before decay. Thus there are essentially three free parameters in this model, namely the running coupling constant of QCD, α_s and Q_o and Q_h. This process is shown schematically in fig. 2. More recently, Webber [10] has introduced interference effects between the showering partons. At present the application of these models to deep inelastic μ-N scattering meets with several theoretical problems and only the aspect of the interference effects of the Webber model will be addressed here. The model is discussed further in section 4.5.

Finally the "firestring" model of Preparata et al., [11] offers an alternative approach to the QPM-QCD methods above. Here hadrons are made of a small number of quarks and antiquarks confined within space-time domains of dimensions which depend upon the mass of the state. No dynamical gluons are invoked in this model. The basic interaction mechanism for ℓ-N scattering is shown in fig. 3; the current is absorbed by an excited quark-antiquark pair which then fragments to hadrons, leaving an excited baryon state. There is an additional 2-firestring diagram which contributes at low x_{Bj}. This leading backward baryon mechanism explains the approximately 50% missing momentum observed in the F_2 structure function measurements.

This paper is organised as follows: Section 2 gives a description of the experimental set-up and of the procedures used to obtain the final event sample. In section 3 the track selection criteria and the acceptance corrections applied to the data are discussed. The presentation of the results in section 4 will start with a study of the p_T distributions and of the balance of p_T amongst the hadrons (section 4.1). The development with W is compared with the predictions of various versions of the Lund model as defined in table 1. These different parameter combinations are chosen to pinpoint the contributions of the various processes in the model and to see whether some aspects of QCD can be equally well replaced by increasing either the primordial transverse momentum, k_T, or the fragmentation transverse momentum scale, σ_q. Comparison is also made with the IJ model predictions.

The Q^2 dependence of the p_T distributions is investigated in section 4.2. In section 4.3, the evidence for QCD effects in the shape of the energy flow distributions and in the jet profiles is discussed. A comparison of the string and IJ models is also made using the jet profiles. With evidence for hard QCD processes firmly established in the earlier sections, attempts at separating three-jet from two-jet events, as well as some properties of the enriched three-jet sample, are discussed in section 4.4.

The effects of soft gluon interference in the fragmentation process are analysed in section 4.5, along with a comparison of the present data with the results of a similar analysis of e^+e^- annihilation measurements in the TASSO detector at PETRA [12].

Finally, in section 4.6 the firestring model predictions for p_T distributions are compared with the data. Section 5 gives the summary and conclusions. Previous work on the analysis of transverse momenta and jet properties can be found in reference 13. These come from an earlier phase of the EMC programme, in which only hadrons which were forward going in the cms system were detected, and also from an analysis based on only part of the sample discussed here.

Table 1

The parameter settings used in the various versions of the Lund model used for comparison with the data

	Hard QCD	Soft Gluons	$<k_T^2>$ (GeV)^2	σ_q (GeV)
A	on	on	$(0.44)^2$	0.44
B	off	on	$(0.44)^2$	0.44
C	on	off	$(0.44)^2$	0.44
D	on	off	$(0.88)^2$	0.44
E	off	on	$(0.44)^2$	0.88
F	off	on	$(0.44)^2$	0.50

2. DESCRIPTION OF THE EXPERIMENT AND DATA

The data presented here were recorded by the EMC (NA9) experiment, in the M2 muon beam at the SPS at CERN. This experiment consisted of a vertex magnet containing a streamer chamber and a 1 metre long liquid hydrogen or deuterium target, large angle track chambers and a forward spectrometer, which was used to detect and measure the scattered muon and fast charged hadrons. The complete system detected tracks from energies of 280 GeV down to less than 200 MeV and gave almost 4π coverage in the hadronic cms. In addition, time-of-flight hodoscopes plus four threshold Cerenkov counters gave good particle identification over a wide range of momenta. More details of the experimental set-up and analysis procedures can be found in references [14,15].

The streamer chamber pictures were measured for all events where the reconstructed scattered μ satisfied the trigger conditions (the main requirement being that the scattering angle of the muon was greater than 0.5°) and these measurements were then passed through the geometrical reconstruction programs. The streamer chamber tracks (SC) covered the low momentum or large emission angle part of the particle spectrum which represented on average 70% of all tracks. The high momentum, small angle tracks were generally not measurable in the streamer chamber as they were obscured by extra beam tracks occurring within the live time of the chamber. These hadron tracks were detected in the forward spectrometer (FS) and reconstructed starting from the most downstream drift chambers placed after the FS-magnet. The large angle part of the spectrometer fulfilled two functions: firstly to improve the parameters of the SC-tracks and FS-tracks and secondly to reconstruct those tracks which were not measured in either the streamer chamber or the forward spectrometer. The primary vertex position was used as an extra constraint in the reconstruction of these large angle spectrometer tracks (called vertex-system (VS) tracks), which contributed mainly to the intermediate region of the particle momentum spectrum.

As the primary vertex was not visible in the streamer chamber, the main vertex position was obtained by fitting the incident and scattered muons and the reconstructed SC and FS tracks to a common interaction point. A search for V° decays and γ conversions, as well as for secondary interaction vertices, was also made amongst the charged hadron tracks detected in the FS and SC. Only such tracks assigned to the primary vertex were used for the analysis presented here. The large angle spectrometer tracks were required to be observed in at least two detectors. Additional checks were made to eliminate tracks being counted in more than one class (FS, SC or VS) and to remove tracks with poor momentum measurements.

The kinematic cuts defined in terms of the deep inelastic scattering variables were as follows:

$$Q^2 > 4\ \mathrm{GeV}^2,$$
$$4 < W < 20\ \mathrm{GeV},$$
$$20 < \nu < 260\ \mathrm{GeV},$$
$$E_\mu' > 20\ \mathrm{GeV},$$
$$y < 0.9,$$
$$\theta_\mu > 0.75^\circ,$$

where E_μ' is the energy of the scattered muon in the laboratory system and θ_μ the scattering angle. These cuts were applied in order to avoid regions where corrections for the acceptance, radiative effects or smearing are large. The number of events remaining after these cuts was about 23,000 in hydrogen. The corresponding sample in deuterium contained 18,000 events, but unless stated to the contrary the analysis refers to the hydrogen data alone.

3. ACCEPTANCES AND TRACK SELECTION

The distributions presented below were corrected for acceptance losses, detector inefficiencies, incorrect vertex assignments and radiative effects. A detailed Monte Carlo simulation of the experiment was performed in which events were generated using the Lund string model [6], imposing the kinematic cuts described above. A simulation of the raw data was made, including simulation of the film measurements, as well as the effects of chamber and hodoscope inefficiences. The tracks produced by γ conversions, K°_s, Λ and $\bar{\Lambda}$ decays and secondary interactions of hadrons in the target were also added to the simulated events.

The reliability of the Monte Carlo simulation was checked in two ways: firstly, the distributions of all kinematic quantities such as Q^2, W^2, and the momentum and angular distributions of hadrons in the laboratory were compared to those measured. Secondly, comparisons were made between the predicted and observed distributions of hits in the reference planes of the detectors.

Apart from enabling the study of distributions of different particle types [16], particle identification also ensures the proper assignment of mass, which is needed for the transformation from the laboratory to the cms system. This boost can only be carried out if the particle mass is known. Particles having ambiguous mass assignments or no particle identification information are treated as follows: all non-identified negative particles are assumed to be pions; positive non-identified particles with $x_F^\pi>-0.2$ are assumed pions as are those with $x_F^\pi<-0.2$ if $x_F^p<-0.9$. (x_F^π is the value of x_F calculated assuming a pion mass, x_F^p is calculated assuming a proton mass); finally, positive non-identified particles with $x_F^\pi<-0.2$ and $x_F^p>-0.9$ are assigned the proton mass. These criteria were developed in order to reduce to a minimum the final correction for misidentified particles, and were derived using Monte Carlo calculations [17].

The Monte Carlo, in general, reproduced the data reasonably well. However, the exact partition into the various track types was not well reproduced and this may lead to a residual uncertainty in the method of acceptance correction. These uncertainties have been extensively studied by altering the various selection criteria and comparing the results obtained after the acceptance correction. The systematic errors on any distribution are estimated to be smaller than or comparable with the statistical errors. Where included, the estimated systematic errors are shown if they are larger than the statistical error. A detailed account of the study of possible systematic effects in the data can be found in references [5,17,18].

4. THE RESULTS

The distribution of the selected events in the Q^2-ν plane, within the kinematic limits and cuts applied to the measured events, is shown in fig. 4. The distribution of muon energies in the beam was centered on 280 GeV and had a width of ± 5%. Lines of constant x_{Bj} and W are included in the plot. The data are seen to be strongly peaked at low Q^2 and x_{Bj} and rather evenly distributed over the available range of ν and W^2. Finally, a contour is overlaid indicating the region where the cross-section for QCD three jet events (as defined in the Lund model) is calculated to be more than 20% of the two jet cross-section.

4.1 p_T Distributions

In fig. 5 differential distributions of a) p_T^2 and b) p_L^2 for forward (x_F>0) and backward (x_F<0) particles are shown separately. That the forward and backward jets may be meaningfully separated by this selection was shown in [19]. The transverse momentum distribution is much narrower than that of the longitudinal momentum, as expected in the parton model. The forward hadrons are observed to have higher transverse momenta than the backward hadrons.

In fig. 6 the mean p_T^2 as a function of W is plotted for forward and backward particles separately, with the central region ($|x_F|<0.2$) excluded. The mean p_T^2 for forward hadrons is seen to increase strongly with W, whilst for the backward hadrons no such W dependence is seen. This effect remains with the central region included, albeit somewhat weaker. The curves in these figures are from the standard Lund model (A in table 1), which as can be seen reproduces the p_T distributions reasonably well. In the forward direction however, the predicted longitudinal momentum distribution is somewhat harder than that observed.

The comparison of forward and backward transverse momenta can be investigated further in the "seagull plot" of $\langle p_T^2 \rangle$ against x_F, shown in fig. 7, which clearly demonstrates the asymmetry between the two hemispheres.

There are several sources of p_T which may give rise to this asymmetry. Forward hadrons have high laboratory momenta and hence may be more susceptible to measurement error. Studies of this effect [17] indicate a very small contribution to the asymmetry. The estimated systematic uncertainty on $\langle p_T^2 \rangle$ is less than or equal to the statistical error. The effect of the backward jet, which results from the target remnants, was investigated by replacing the target remnant system by an antiquark in the Lund Monte Carlo program. This was found to give a negligible $\langle p_T^2 \rangle$ asymmetry. Gluon radiation is however, expected to increase the struck quark transverse momentum, whilst having a negligible effect on the target jet. In fig. 7 several curves are drawn indicating the relative contribution to the seagull plot within the Lund model. The dominant contribution to the asymmetry is found to be the soft gluon component, to which hard QCD processes contribute in some measure at medium values of positive x_F. Using a large value of the transverse Fermi momentum, $<k_T^2>=(0.88\ \mathrm{GeV})^2$, but without using soft gluons, the $<p_T^2>$ in the forward direction are reproduced. However, this increases the $<p_T^2>$ in the backward direction in a symmetric way and is incompatible with the data. It should be noted that the specific method used to implement the soft gluon effects in the LUND model is not uniquely defined in QCD but relies on some particular prescriptions.

For the independent jet models considered, only the hard QCD processes can give rise to the forward/backward asymmetry of the $<p_T^2>$. However, increasing the contribution of these processes causes a distortion in the region of small positive x_F, in disagreement with the data as seen in fig. 8.

In order to study correlations in transverse momenta, a measure of the manner in which the leading forward and backward hadron transverse momentum is balanced has been obtained. We define a leading forward trigger particle as one with $x_F>0.5$ and a leading backward particle as having $-0.5<x_F<-0.2$ (a very backward trigger, having $x_F<-0.5$ was not used to avoid any problems of low acceptance in this region). The component of the momentum balancing that of the trigger for all other hadrons i, is

$$p_{T_i}' = p_T \cos\phi_i$$

where ϕ is the azimuthal angle in the cms system around the virtual photon direction with ϕ (trigger)=0. Hence the balancing momentum flow is

$$\frac{dp_T^{bal}}{dy^*} = \frac{1}{N_{eV}} \int p'_T \frac{d^2N^{bal}}{dp'_T dy^*} dp'_T$$

and is plotted in fig. 9. The rapidity range where the trigger particle is found is indicated. Besides the standard LUND model (model A) curves, which reproduce the data well, curves obtained from this model without soft gluon emission (model C) and with increased $<k_T^2>=(0.88\ \mathrm{GeV})^2$ (model D) are included to show the different contributions.

The primordial k_T, being equivalent to a rotation of the event axis away from the current direction leads to a balancing of the forward trigger particle p_T in the backward region and vice versa. The forward trigger particle will predominantly contain the struck quark, thus the soft gluon radiation, as implemented in the LUND model, will balance p_T over the available rapidity range. The data rule out large values of k_T and are better fitted with the soft gluon component included.

Figure 10 shows the p_T balance plot, with the predictions of the two independent jet models overlaid. The pronounced dip in the central rapidity region for these models is indicative of the independence of the jets, however, it is seen that the momentum conservation scheme employed in the different models has an important effect. In neither case can the data be adequately reproduced by the model curves, especially for the p_T balance of the backward trigger particle.

Hard QCD processes, resulting in a tendency towards 3-jet events are expected to be manifest in the form of planar event shapes. In order to study this effect we define an event plane from the measured hadrons. The event plane is constrained to contain the virtual photon vector. The orientation of the plane about this axis is then obtained by minimising the hadron momentum component transverse to the plane (p_T^{out}). This prescription is equivalent to maximising the transverse momentum component within the plane (p_T^{in}).

Figures 11a and b, display the differential distributions, for events containing two or more charged hadrons, of $\Sigma(p_T^{in})^2$ and $\Sigma(p_T^{out})^2$ respectively. The distribution in the plane is much harder than that out of plane. Some component of this effect is an artefact of the procedure for defining the event plane, coupled with the limited multiplicity of the data. However, the failure of the 2-jet model to reproduce the data indicates the underlying planar nature of the events. Evident from this plot is the small effect of soft gluon radiation on the tail of the p_T^2 distribution within the event plane (the dotted curves is the Lund model without soft gluon emission). The dashed curve is the Lund model without hard QCD and with the fragmentation p_T parameter σ_q increased 10%. The dot-dashed curve is again for no hard QCD but with σ_q=0.88 GeV/c. In conclusion it is not possible to account for the tail of this distribution by increasing the fragmentation transverse momentum only.

4.2 Q^2 Dependence of Transverse Momentum Distributions

In the above section it has been shown that $<p_T^2>$ depends on the cms energy W. In this section the possible dependence on Q^2 is investigated. For each interval of Q^2 there is a different range of W values and the mean W falls with increasing Q^2. Hence there is an inherent Q^2 dependence due to the W dependence. In order to minimise this, the data was divided into four ranges of W and each of these W intervals was subdivided into two intervals of Q^2, corresponding to low and high Q^2 for that W interval. Table 2 shows the intervals of W and Q^2 used.

Table 2

Values of low and high Q^2 used for the various W intervals

W range	low Q^2 range	High Q^2 range
$W \leq 8$ GeV	$Q^2 \leq 30$ GeV^2	$Q^2 > 30$ GeV^2
$8 < W \leq 12$ GeV	$Q^2 \leq 20$ GeV^2	$Q^2 > 20$ GeV^2
$12 < W \leq 16$ GeV	$Q^2 \leq 20$ GeV^2	$Q^2 > 20$ GeV^2
$16 < W < 20$ GeV	$Q^2 \leq 10$ GeV^2	$Q^2 > 10$ GeV^2

The method used to search for any Q^2 dependence was, for a given W range, to divide the $\langle p_T^2 \rangle$ found at high Q^2 by that found at low Q^2, in intervals of x_F. The data in the backward hemisphere show no significant Q^2 dependence. The data in the forward hemisphere are shown in fig. 12. From QCD it is expected that $\langle p_T^2 \rangle$ is proportional to $\alpha_s(Q^2)$ and hence should decrease with increasing Q^2 at fixed W. An estimate of the expected magnitude of the effect is also shown in fig. 12. The lines shown are computed using the Lund model. The dashed line corresponds to a version of the model with no hard QCD (model B) and it can be seen that this predicts an increase of the ratio with increasing x_F. The size of this increase diminishes as W increases. When hard QCD effects are included (solid line), using a value of Λ=300 MeV (model A), the prediction is that the ratio decreases with increasing x_F, as expected. The errors on the data are, however, too large to distinguish between these versions of the model.

Figure 13 shows the ratio of the differential p_T^2 distributions for high and low Q^2. The data is divided into two regions of W, namely W≤12 GeV and W≥12 GeV and each W region is subdivided into two regions of x_F. In all cases the division between high and low Q^2 is 20 GeV^2. The data are reasonably well reproduced by the Lund model which includes hard QCD effects (solid line, model A), but rather less well by a version of the model without hard QCD effects (dashed line, model B). The systematic error on the ratio due to the change in the smearing of the current direction as a function of W is estimated to be about 15%.

In summary no significant variation of the p_T distributions with Q^2 at fixed W is observed. Such a variation would be expected from QCD due to the change of α_s with Q^2. The size of the expected change with Q^2 depends on the value of Λ and for values of $\Lambda \lesssim 0.5$ GeV the data is not precise enough for this effect to be observed. However, large values of Λ ($\gtrsim 1$ GeV^2) can be ruled out.

4.3 Energy Flow

Within the event plane, a study of the hadronic energy flow can be made to search for evidence of 3-jet structures. The normalised cms planar energy flow is defined as

$$\frac{dE(\theta)}{d\theta} = \int \frac{E_i}{W} \frac{d^2N}{dE_i d\theta} dE_i$$

where i runs over all charged particles in the event. θ_i is the angle between the current (γ*) direction and the direction of the i^{th} hadron projected into the event plane, with $\theta=0°$ corresponding to the current direction. The sense of θ, is defined for each track such that the track with the largest p_T has $\theta<0°$. This analysis only includes events with at least four forward going ($x_F>0$) charged hadrons. 9093 events passed this cut. Figure 14 shows the planar energy flow for these events. A simple requirement expected to enhance the fraction of hard QCD events is to consider only events containing a hadron with p_T^2 greater than some minimum value. For a minimum p_T^2 cut of 1.5 and 2.5 $(\mathrm{GeV}/c)^2$, the remaining sample contain 357 and 105 events respectively. The energy flow for these samples is shown in figs. 15 and 16.

The curves for model E (no hard QCD, $\sigma_q=0.88$ GeV) compare reasonably with the data in fig. 15, becoming more disfavoured in fig. 16. The data without any p_T^2 cut (fig. 14) is also poorly reproduced by these conditions. The curves shown in figs. 14, 15 and 16 are all normalised so that their integrals are the same as that of the data. However, the model without hard QCD predicts an absolute fraction of events passing the above criteria which is much smaller than that in the data.

Taken together with the $p_T^2(\mathrm{in})$ and $p_T^2(\mathrm{out})$ distributions, these plots show that simple 2-jet models, containing no hard QCD and with a gaussian fragmentation p_T distribution, are unable to reproduce the data.

In order to separate QCD effects in jets from purely kinematic effects, we have studied the scaled energy flow [20,21] defined by

$$\frac{d\varepsilon}{d\lambda} = \rho(\lambda) = \frac{1}{N_{ev}} \ \Sigma \ \frac{\Delta\varepsilon_i}{\Delta\lambda} ,$$

where $$E_{jet} = \Sigma \ E_i^{charg} \ , \quad \varepsilon^i = E_i^{ch}/E_{jet}$$

and $$\lambda = \frac{x_F}{p_t} = \frac{\cot\theta}{W/2} \quad .$$

The quantity θ is the angle between the hadron and the virtual photon and E_i is the cms energy of the i^{th} charged hadron. This jet profile was found to scale (i.e. be independent of jet energy) in low energy pp reactions [20], in neutrino-proton [22] and K^+ proton [23] scattering. Such scaling is expected in cascade models of fragmentation. We have analysed the data in four W intervals (W_1:4-8 GeV, W_2:8-12 GeV, W_3:12-16 GeV and W_4:16-20 GeV) and compared the results to model predictions. In this analysis events are included only if they have at least one forward and one backward going hadron.

Figure 17 shows the distributions in four intervals of W for both the forward and backward jets. Except for the first bin, the data in the backward hemisphere is roughly independent of W, whereas in the forward hemisphere there is a marked W dependence, the distribution becoming more peaked toward $\lambda=0$ as W increases.

To illustrate the W dependence we take the ratio

$$R_{ij} = \frac{(d\varepsilon/d\lambda)_i}{(d\varepsilon/d\lambda)_j}$$

of the distribution in the first W interval to those in each of the higher W intervals, and these are plotted in fig. 18. Also shown in fig. 18 are the expected distributions from the independent jet model. Without QCD this model gives reasonably good scaling in W, for both the backward and forward jets. Including QCD effects in the model gives rise to scaling deviations, but still fails to describe the data for higher values of W. Increasing the value of Λ improves agreement in the forward direction, but at the expense of worse agreement in the backward direction.

The same ratios of energy profiles are compared to the Lund model predictions in fig. 19. While the backward jet ratios essentially remain flat, with and without hard QCD included, the forward jets show sizeable deviations increasing with W. These deviations in the model are due to hard QCD as well as to multiple soft gluon emission, these effects being almost equally large. In contrast to the IJ model, there are scaling deviations present already in the Lund model without QCD. In fact this behaviour is expected as a "string-effect" due to a "crosstalk" between the backward and the forward jet. The x_F distribution of the forward going particles depends on the transverse mass of the backward going particles (baryons from the target remnant) and explains part of the scaling deviations associated with the lowest W interval in the string model [24]. By definition, there is no "crosstalk" in independent jet fragmentation. Reasonable agreement between the data and Monte Carlo can only be obtained using the Lund string fragmentation, including the effects of QCD.

For a quantitative analysis we have fitted the suggested radiation profile function [20]

$$\rho(\lambda) = \frac{M}{(1+(\lambda M)^2)^{3/2}}$$

to the data in fig. 17. It has been shown that this distribution roughly fits the low energy data and has the correct behaviour for $\lambda \to 0$ and $\lambda \to \infty$ ($\rho(0)=M$; $\rho(\infty)=0$). It can be seen from fig. 17 that $\rho(\lambda)$ gives a reasonable description for the forward region. Due to crossover between forward and backward hemisphere the fit has been made for $\lambda > 0.2$ only. The backward jet, however, shows sizeable deviations, due to the much more complicated target remnant system fragmenting.

The variation of the transverse mass parameter M can be used as a measure of the observed scaling deviations. In fig. 20, the values of M found are plotted against W and compared to various Monte Carlo predictions, computed with different values of the QCD scale parameter Λ and of the fragmentation transverse momentum parameter σ_q.

If the Lund fragmentation scheme is used to model non-perturbative effects, a value for Λ can be determined from fig. 20 and from the ratios of fig. 19. This value can be expressed in terms of α_s using the leading order QCD formula

$$\alpha_s(Q^2) = \frac{12\pi}{(33-2n_f)\log(Q^2/\Lambda^2)}$$

giving

$$\alpha_s(Q^2{=}20\ \mathrm{GeV}^2,\ n_f = 4) = 0.29 \pm 0.01_{\mathrm{stat.}} \pm 0.02_{\mathrm{syst.}}$$

where the systematic error does not include the uncertainty from the fragmentation model.

However, the Independent Jet Model fails to describe the data even with a value of Λ larger than 1 GeV.

4.4 Search for Three-Jet Events

With evidence for hard QCD processes in the data, several different attempts were made to separate these 3-jet events from the 2-jet events and then to reconstruct the jet momentum vectors.

The subset of events having at least one hadron with p_T^2 larger than 2.5 $(GeV/c)^2$ as used in fig. 16, for example, contains 105 events out of the total sample of about 23,000. Figure 21 shows some calculations made using the Lund model on the fraction of $q\bar{g}$ and $q\bar{q}$ 3-jet events as a function of the p_T^2(max) cut on the forward hadron used to select the sample. It can also be seen that a reasonably clean sample of 3-jet events can be selected, however, only at the expense of severely restricting the sample size. It can also be seen that the two hard QCD processes make comparable contributions to the total number of 3-jet events. Imposing a cut $x_{Bj}>0.06$, in order to enrich the fraction of qg events, gives a factor of qg to $q\bar{q}$ events of about two to one for $p_T^2(\max)>1.5$ GeV^2, again at the expense of reducing the total sample by a further factor of two.

A cluster algorithm was developed as an alternative approach to the method of applying a cut on (p_T)max. A search was made for events which had three separated clusters, each cluster having tracks with small angles between their momentum vectors in the CMS. The cluster algorithm applied here [25] is similar to the procedure described in [26]. Since, as discussed above, the backward jet is rather narrow, all backward going hadrons were assumed to form one cluster. The algorithm was then only applied in the forward hemisphere. It was tuned on the basis of the results from the Monte Carlo simulations in order to reach the optimum between high efficiency for finding 3-jet events and low contamination from 2-jet events. With the final set of parameters, the contamination from 2-jet events is reduced to 24% in the selected sample, which contains 2.5% of the original 3-jet events.

The data sample used in this analysis comprises events from both the H_2 and D_2 targets. In addition to the cuts on the event variables given in section 2, the sample was further restricted to the W range between 10 and 20 GeV. It was also required that there was at least one charged hadron in the backward cms hemisphere and more than three charged hadrons going forward. In total 12,400 events fulfil these criteria. From the Monte Carlo studies discussed above one expects to obtain about 110 3-jet events, with an estimated contamination of about 25 2-jet events. Application of the cluster algorithm to the data yields 118 events, a number which is in agreement with the expectation.

In fig. 22 the p_T^2 distribution of forward going charged hadrons from the 3-jet events is shown, normalised to the number of events in this sample. For comparison the distribution is also included for the 2-jet events (containing 12% contamination from 3-jet events) found by the same cluster algorithm. The p_T^2 distribution for 3-jet events is clearly broader than the one for 2-jet events. The values of $\langle p_T^2 \rangle$ are $(0.56\pm0.01)\mathrm{GeV}^2$ and $(1.72\pm0.17)\mathrm{GeV}^2$ for 2 and 3-jet events respectively. When interpreting this big difference one has to keep in mind that the cluster algorithm imposes a strong bias on the 3-jet sample. It was found by Monte Carlo studies that the cluster algorithm increased $\langle p_T^2 \rangle$ of 3-jet events by 0.38 GeV^2. This bias is not sufficient to explain the entire difference between the $\langle p_T^2 \rangle$ values of the 2 and 3-jet samples. So one can conclude that the 3-jet events exhibit a significantly higher value of $\langle p_T^2 \rangle$ than the 2-jet events.

The yields of forward going protons and antiprotons have been determined for the 2 and 3-jet samples. The fractions of $p+\bar{p}$ among all charged hadrons in the forward hemisphere are found to be $(8.3\pm0.2)\%$ and $(12.7\pm2.5)\%$ for the 2 and 3 jet events respectively. This indicates a more copious $p+\bar{p}$ production in 3-jet events. As these events show significantly higher p_T^2 values, this finding is at least qualitatively in good agreement with the observation [27] that $(N^{\bar{p}}+N^{p})/(N^{h+}+N^{h-})$ increases with increasing p_T^2.

4.5 Soft Gluon Interference

The cascade model of Webber includes the effects of interference between parton showers. Interference effects of a similar nature are known to occur in QED. For example, a long wavelength bremsstrahlung photon emitted at large angles in e^+e^- pair production cannot resolve the e^+ and e^-. The photon is therefore emitted coherently by the e^+e^- pair. Since the electron pair has an effective total charge of zero the rate of emission is suppressed. Calculations show that there is an ordering of the angles of emission which has the effect of strongly reducing the number of such soft photons emitted at small angles [28,29].

The case of QCD is complicated by the fact that gluons carry colour charge. However, recent calculations [30] in the domain of semi-hard QCD have shown that an effect similar to that in QED does exist. A soft gluon emitted at large angle cannot resolve individual colour charges within a jet as it is sensitive only to the total colour charge. A similar ordering condition on the angles of the emitted gluons leads to a reduction in the number of emitted soft gluons, as in the QED case for the emitted soft photons. The calculations also include further destructive interference between different multigluon graphs which have no QED analogue, hence the name of the soft gluon interference effect.

QCD calculations of e^+e^- annihilation into partons through the mediation of a virtual photon of four-momentum squared Q^2 give clear predictions [30,31] for the distribution of the emitted gluons. The number of soft gluons is strongly reduced and the shape of the distribution $xd\sigma/dx$ plotted as a function of $\ln(1/x)$ is asymptotically gaussian for large Q^2 with a maximum at $(1/4)\ln(Q^2/Q_\circ^2)$. The quantity $Q_\circ$ is an infrared cut-off and x is the momentum fraction (of Q/2) carried by the parton. QCD calculations are only reliable if the masses of the final state gluons are larger than Q_0, typically 0.7 GeV. Hence a linear variation of the position of the maximum of the distribution $x d\sigma/dx$ with $\ln Q^2$ is predicted, with a slope of 0.25 [31]. Without the soft gluon interference effect, and as $Q \to \infty$, this slope would be expected to be 0.5.

The Webber Monte Carlo model was developed to study e^+e^- annihilation. For comparison with deep inelastic muon-proton scattering it was modified to simulate the flavour ratio of the forward scattered quarks. Only forward hadrons are studied to avoid contamination from the remnant diquark fragmentation, which is not included in the model. In these calculations the momentum fraction of the parton, x, has been replaced by $x_p=2p/W$, the momentum fraction of the hadron. Investigation with the model indicated that while the slope of the variation of the maximum of the distribution $x d\sigma/dx$ with $\ln Q^2$ is strongly changed for pions by a large contamination of higher mass resonance decay products, this is not so for kaons and protons in the centre of mass energy range of this experiment ($4<W<20$ GeV). Thus the slope obtained for these particles serves as a more reliable test of the soft gluon interference mechanism.

The identified forward charged pions, kaons and protons were were divided into different bins of W, and for each W bin the distribution $x_p d\sigma/dx_p$ was plotted against $\log(1/x_p)$, where $x_p=2P/W$ and P is the hadron momentum in the centre of mass frame. As an example, some distributions are shown in fig. 23. More details of this analysis can be found in ref. [32]. The position in $\ln(1/x_p)$ of the maximum of each distribution was determined for each W bin by fitting a gaussian to the distribution. Figure 24 shows the variation of the position of this maximum with W^2 from the data, compared with the predictions of the Lund [6] and Webber [10] Monte Carlo models and with the results obtained by TASSO [12]. Straight line fits were made to the EMC data for each particle type in fig. 24. Table 3 gives the results of the fits together with the predictions of the two models.

The slopes for the Webber model given in table 3 show that for both kaons and protons the values are close to 0.25, the value expected from the soft gluon interference effect. This shows that the hadronisation process, at least in this model, does not distort this effect for heavy particles. The Lund model, on the other hand, which does not include this effect, predicts a somewhat larger slope for kaons but a slope for protons which is similar to that of the Webber model. For pions, the Webber model predicts a slope which is different from 0.25, indicating that for such low mass particles the hadronisation process distorts the effects of soft gluon interference.

Table 3

Slopes of the straight line fits to the position $\ln(1/x_p)$ of the maximum of $x_p d\sigma/dx_p$ as a function of W^2 (fig. 24).

Slopes	Pions	$K^\pm$	K°	Protons
EMC Data	0.42±0.01±0.02	0.29±0.06±0.09	0.36±0.12±0.10	0.21±0.05±0.06
Lund Monte Carlo	0.38	0.43	0.35	0.23
Webber Monte Carlo	0.32	0.26	0.24	0.25

It can be seen from table 3 and fig. 24 that the data for pions and protons are in reasonable agreement with both the Webber and Lund models. For charged kaons the slope of the data agrees well with the prediction of the Webber model but is somewhat smaller than that predicted by the Lund model. However, the difference is mainly due to the low W region where the corrections for experimental acceptance are largest. The neutral kaons data have larger statistical errors and are compatible with both models.

4.6 Comparison with Firestring Model

As discussed in the introduction an alternative to the QCD based models is the Firestring model [11] in which the concept of quarks and confinement is retained but the QCD idea of dynamical gluons is rejected.

The model reproduces the measured F_2 reasonably well and has been compared with the forward and backward charged particle multiplicities ($n_F^{\pm}$ and $n_B^{\pm}$) as well as to the identified hadron inclusive x-Feynman distributions elsewhere [33]. There it was found that the predictions agreed reasonably well with the data except for $n_F^{\pm}$ at high W and $n_B^{\pm}$ at low W. Some problems were found in reproducing the pion and kaon distributions in the negative x_F region as well as the proton distribution. This latter problem appears to be a reflection of the leading baryon mechanism which is central to the model and thus has potentially the most serious consequences. Here we explore the model predictions for the jet variables already discussed above.

Figure 25 shows the inclusive $\Sigma(p_T^{in})^2$ distribution for the data along with the prediction of the firestring model. Reasonable agreement between model and data is observed; however, the model predicts a greater yield at $p_T^2 \gtrsim 3$ GeV^2 than is observed. The plot of $<p_T^2>$ versus x_F in fig. 26 indicates that, while the model gives some forward-backward asymmetry in the p_T distributions, the magnitude of the effect is significantly greater in the data than in the model. The study of the balance of transverse momentum as described above has also been applied to the firestring model. It can be seen that with both forward and backward trigger particles the transverse momentum is balanced centrally around $y^*=0$ (fig. 27). This provides an adequate description of the balancing of the forward trigger particles; but the balancing of backward going trigger particles is markedly different from the data.

5. SUMMARY

A detailed study of hadronic jet production in deep inelastic muon-nucleon scattering has been performed with emphasis on distinguishing between various fragmentation models. In particular high statistics data on inclusive p_T distributions, transverse momentum balance and hadronic angular energy flow have been presented. Within the models analysed, an investigation was made of the relative importance of the initial scattering process and the hadronisation in several different aspects of the data. In this way strong limitations have been placed on the available models.

Data presented on the average p_T^2 as a function of x_F (the "seagull plot") have shown the inability of the independent jet models to reproduce the observed forward backward asymmetry. Within the Lund string fragmentation model, it has been found that the soft gluon component of the transverse momentum is primarily responsible for the observed asymmetry. The Lund model satisfactorily reproduces the measured seagull plot.

The data presented on the manner in which the transverse momentum of a trigger particle is balanced by the remaining particles in any given interaction, limit the magnitude of the primordial quark transverse momentum. The Lund model is also much favoured over independent jet models in this analysis, with the leading forward and backward trigger particle transverse momentum being balanced centrally.

The inclusive p_T^2 distribution both within and perpendicular to the event hadronic plane are essentially unaffected by the inclusion of soft gluon effects and thus constitute evidence that the planar structure observed in the data is due to hard QCD processes. The data also impose limits on the magnitude of the fragmentation induced p_T.

The average p_T^2 is found to increase with the hadronic cms energy W, more rapidly than does the longitudinal momentum component. At fixed W no significant Q^2 dependence of the average transverse momentum is found, placing an upper limit on the first order QCD parameter $\Lambda \lesssim 0.5$ GeV.

The measured angular hadronic energy flow within the event hadronic plane is consistent with the models investigated, provided the "hard" QCD processes are included. A detailed study of the jet profiles favour the string model over the independent jet model. These studies were also used to extract, in leading order, a value of $\alpha_s = 0.29 \pm 0.01$ (stat.) ± 0.02 (syst.), for a value of $Q^2 \sim 20$ GeV^2 and using the Lund string model. The systematic error quoted does not include the uncertainties due to the choice of this fragmentation model.

Enriching the three-jet sample of events via a cluster algorithm leads to evidence for increased $\langle p_T^2 \rangle$ in these events beyond that imposed by the selection process. Proton and anti-proton multiplicities are also higher in this sample.

Studies of the behaviour of the distributions $x_p d\sigma/dx_p$ as a function of W show that the data are compatible with the QCD cascade model of Webber, which includes soft gluon interference effects, but also with the Lund string model which does not.

Beyond the problems described elsewhere [33] of the "firestring model" in reproducing the proton x_F distributions, this model does reproduce many of the measured p_T properties. The forward backward asymmetry in $\langle p_T^2 \rangle$ predicted by this model is however smaller than that observed. The balance of transverse momentum is also not well reproduced for backward trigger particles. However, the version of the model used is the first version of this model and has not been tuned in any way to fit the data.

In summary, taken as a whole, the data presented are able to exclude the independent jet fragmentation schemes. The Lund model, with hard QCD processes and soft gluon effects included, satisfactorily reproduces all the measured distributions presented.

Acknowledgements

We wish to thank all the people in the various laboratories who have contributed to the construction, operation and analysis of this experiment. The support of the CERN staff in operating the SPS, the muon beam and computer facilities is gratefully acknowledged. We also thank G. Ingelman, M. Le Bellac, E. Ferrari and B. Webber for helpful and stimulating discussions.

REFERENCES

[1] G. Hanson et al., Phys. Rev. Lett. 35 (1975) 1609;
D.P. Barber et al., Phys. Rev. Lett. 43 (1979) 830;
W. Bartel et al., Phys. Lett. 91B (1980) 142;
Ch. Berger et al., Phys. Lett. 86B (1979) 418;
R. Brandelik et al., Phys. Lett. 86B (1979) 243.

[2] P. Hoyer et al., Nucl. Phys. B161 (1979) 349.

[3] A. Ali et al., Phys. Lett. 93B (1980) 155.

[4] R.D. Field and R.P. Feynman, Nucl. Phys. B136 (1978) 1.

[5] N.I. Geddes, D. Phil. Thesis, University of Oxford (1985) RAL-T-017.

[6] B. Andersson et al., Phys. Rep. 97 (1983) 31;
B. Andersson et al., Z. Phys. C3 (1980) 223;
B. Andersson et al., Z. Phys. C9 (1981) 233;
G. Ingelman, The Lund Monte Carlo for Deep Inelastic Lepton-Nucleon Scattering, LEPTO Version 4.2.

[7] G.C. Fox and S. Wolfram, Nucl. Phys. B168 (1980) 285.

[8] R.D. Field and S. Wolfram, Nucl. Phys. B213 (1983) 65.

[9] T.D. Gottschalk, Nucl. Phys. B214 (1983) 201.

[10] B.R. Webber, Nucl. Phys. B238 (1984) 492;
G. Marchesini and B.R. Webber, Nucl. Phys. B238 (1984) 1.

[11] G. Preparata, Proc. 11th SLAC Summer Institute on Particle Physics 1983, p. 395 (1983).

[12] TASSO collaboration, M. Althoff et al., Z. Phys. C22 (1984) 307.

[13] EMC, J.J. Aubert et al., Phys. Lett. 95B (1980) 306;
EMC, J.J. Aubert et al., Phys. Lett. 100B (1981) 433;
EMC, J.J. Aubert et al., Phys. Lett. 114B (1982) 373;
EMC, J.J. Aubert et al., Phys. Lett. 119B (1982) 233;
EMC, J.J. Aubert et al., Phys. Lett. 130B (1983) 118;
EMC, M. Arneodo et al., Phys. Lett. 149B (1984) 415;
EMC, J.J. Aubert et al., Z. Phys. C34 (1987) 277.

[14] EMC, O.C. Allkofer et al., Nucl. Inst. and Meths. 179 (1981) 445.

[15] EMC, J.P. Albanese et al., Nucl. Inst. and Meths. 212 (1983) 111.

[16] EMC, M. Arneodo et al., Phys. Lett. 150B (1985) 458.

[17] A.S. Johnson, D. Phil. Thesis, University of Oxford (1984) RL-T-119.

[18] K.R. Long, D. Phil. Thesis, Unviversity of Oxford (1984) RAL-T-001.

[19] EMC, J.P. Albanese et al., Phys. Lett. 144B (1984) 302.

[20] W. Ochs, L. Stodolsky, Phys. Lett. 69B (1977) 225;
H. Fesefeldt, W. Ochs, L. Stodolsky, Phys. Lett. 74B (1978) 389;
W. Ochs, T. Shimada, Z. Phys. C4 (1980) 141.

[21] H. Fesefeldt, Aachen PITHA 85-02, Aachen 1985.

[22] P. Allen et al., Phys. Lett. 112B (1982) 88.

[23] I.V. Ajinenko et al., Z. Phys. C16 (1983) 291.

[24] G. Ingelman, CERN-TH 3926 (1984).

[25] D. Teuchert, Diplom Thesis, University of Aachen (1981);
A. Krüger, Diplom Thesis, University of Hamburg (1986).

[26] H.J. Daum, H. Meyer, J. Bürger, Z. Phys. C8 (1981) 167.

[27] EMC, J.J. Aubert et al., Phys. Lett. 135B (1984) 225.
Earlier data on proton production is given in
J.J. Aubert et al., Phys. Lett. 103B (1981) 388.

[28] For a review see M. Le Bellac, Proc. of the 19th Rencontre de Moriond, La Plagne, March 4-10th, 1984, p. 487, ed. by J. Tran Thanh Van and the references therein.

[29] A. Sudakow, Izvestia AN USSR (Fizika) 19 (1955) 650.

[30] A. Bassetto et al., Nucl. Phys. B207 (1982) 189.

[31] A.H. Mueller, Phys. Lett. 104B (1981) 161 and Nucl. Phys. B213 (1983) 85;
Y.L. Dokshitzer et al., Phys. Lett. 115B (1982) 242.

[32] G. D'Agostini, Thèse d'état, Universite d'Aix-Marseille II.

[33] P. Renton, Proc. of the XVIth Int. Symp. on Multiparticle Dynamics, Kiryat Anavim,p. 17 (1985).

FIGURE CAPTIONS

[1] The mechanism of deep inelastic ℓ-N scattering.
(a) The basic QPM diagram and (b) $O(\alpha_s)$ QCD corrections.

[2] The fragmentation process in the QCD parton shower model.

[3] Deep inelastic scattering in the firestring model. FS represents a firestring and B* an excited baryon.

[4] Distribution of DIS events in the Q^2-ν plane. The area to the right of the solid line corresponds to the kinematic region where the ratio of the QCD 3-jet to 2-jet cross section is larger than 20%. Lines of constant x and W are also shown.

[5] Differential (a) p_T^2 and (b) p_L^2 distributions for forward ($x_F>0$) and backward ($x_F<0$) hadrons.

[6] Mean p_T^2 as a function of W^2 for forward and backward hadrons. (The central region, $|x_F|<0.2$, excluded).

[7] $<p_T^2>$ versus x_F compared with predictions of the Lund model (see table 1 for meaning of curves A,B,C,D).

[8] $<p_T^2>$ versus x_F with the predictions of the independent jet fragmentation model of Hoyer for Λ_{QCD}=0.3 GeV and Λ_{QCD}=1 GeV.

[9] Transverse momentum balance dp_T^{bal}/dy^* for (a) forward trigger (b) backward trigger particles. Curves represent predictions from the Lund model (see table 1).

[10] As in [9] with predictions from (a) independent jet model, b) firestring model.

[11] Differential (a) $\Sigma(p_t^{in})^2$ and (b) $\Sigma(p_T^{out})^2$ distributions compared with predictions of the Lund model. (p_T^{in} and p_T^{out} are transverse momentum within, and perpendicular to, the hadronic event plane, respectively). The events are required to have two or more charged hadrons.

[12] Ratio of $<p_T^2>$ for high and low Q^2 versus x_F, for four intervals of W (see table 2). The curves are computed using the Lund model without hard QCD effects (dashed line) and including hard QCD effects (solid line).

[13] Ratios of the differential p_T^2 distributions for different intervals of W and x_F. The curves are the same as for fig. 12.

[14] Angular hadronic cms energy flow within the hadronic event plane. The curves are the predictions of the Lund model (see table 1).

[15] As with fig. 14, but excluding events with $p_T^{2max}<1.5$ $(GeV/c)^2$. The curves are the predictions of the Lund model (see table 1).

[16] As with fig. 14, but excluding events with $p_T^{2max}<2.5$ $(GeV/c)^2$. The curves are the predictions of the Lund model (see table 1).

[17] Differential energy flow $d\epsilon/d\lambda$ for (a) forward and (b) backward hadrons in four ranges of hadronic cms energy, W. The curves show the fits to the distribution $\rho(\lambda)=M/(1+M^2\lambda^2)^{3/2}$.

[18] Ratio of differential energy flows from different regions of W, in comparison with independent jet model predictions. The indices i,j=1,4 which label the W ranges are the same as for fig. 17.

[19] Ratio of differential energy flows from different regions of W, in comparison with Lund fragmentation model predictions.

[20] Fitted values of parameter M defined in the text for different ranges of W. The curves show predictions for both the Lund and independent jet models.

[21] Calculation of enrichment of QCD 3-jet events along with the reduction in total sample size as a function of the maximum p_T^2 cut. Only forward jets are considered, in each case there is a jet corresponding to the target remnant in the backward direction.

[22] Differential p_T^2 distribution for 3-jet and 2-jet events as selected via the cluster approach.

[23] Examples of the scaled differential cross sections $x_p d\sigma/dx_p$ as a function of $\ln(1/x_p)$ for π^+ $K^\pm$ and $p/\bar{p}$ and for various intervals of W. The smooth curves show fits of Gaussian distributions.

[24] The values of $\ln(1/x_p)$ at the maximum of $x_p\, d\sigma/dx_p$ as a function of W^2 for pions, kaons and protons. The curves show the predictions of the Lund (dashed line) and Webber (full line) models. The full squares are the data of TASSO [16].

[25] $\Sigma(p_T^{in})^2$ distribution compared with the prediction of the firestring model (p_T^{in} is the transverse momentum within the event plane).

[26] $<p_T^2>$ versus x_F compared with the predictions of the firestring model.

[27] Transverse momentum balance dp_T^{bal}/dy^* for (a) forward (b) backward trigger particles. Predictions are from the firestring model.

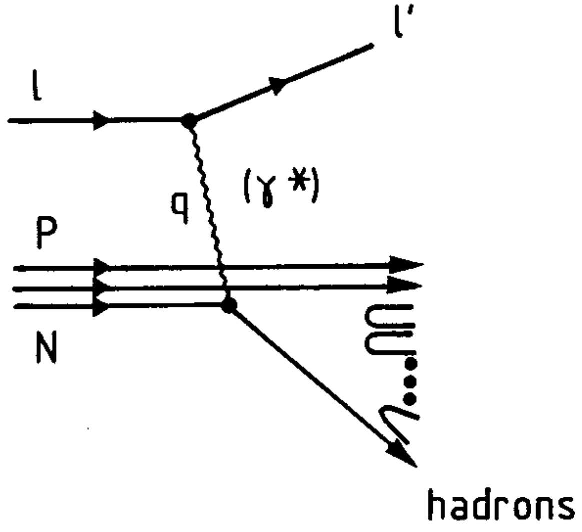
l'
l
(γ^*)
q
P
N
hadrons

FIG. 1a

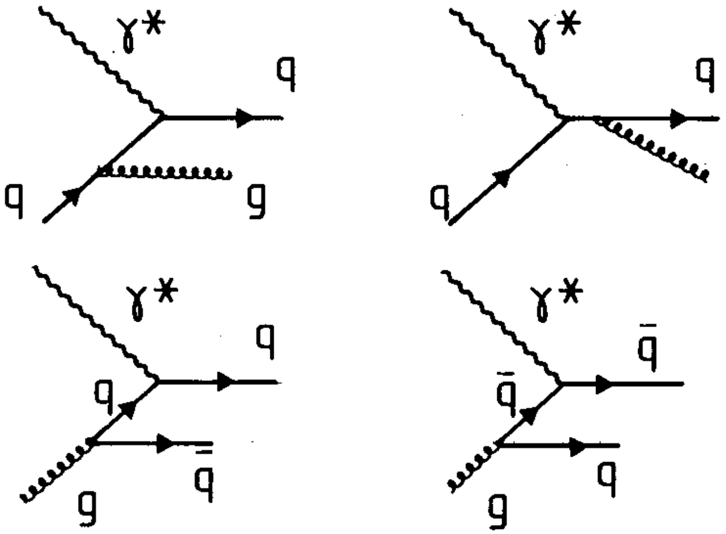
γ^*
q
q
g
γ^*
q
q
γ^*
q
q
g
$\bar{q}$
γ^*
$\bar{q}$
$\bar{q}$
g
q

FIG. 1b

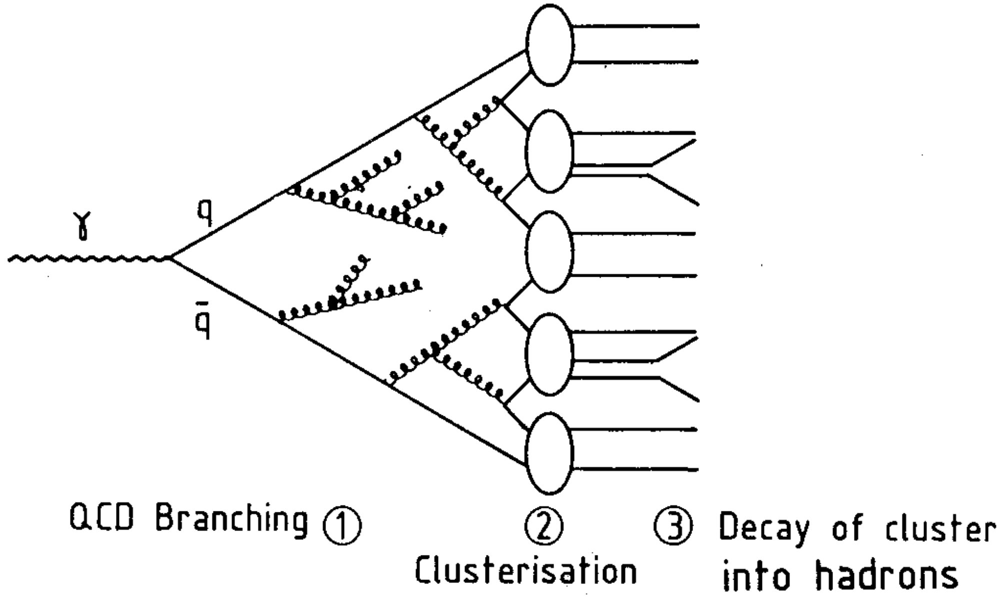
γ
q
q̄
QCD Branching ①
② Clusterisation
③ Decay of cluster into hadrons

FIG. 2

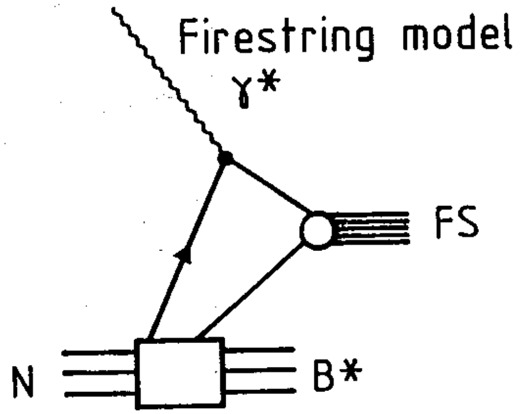
Firestring model
γ*
FS
N
B*

FIG. 3

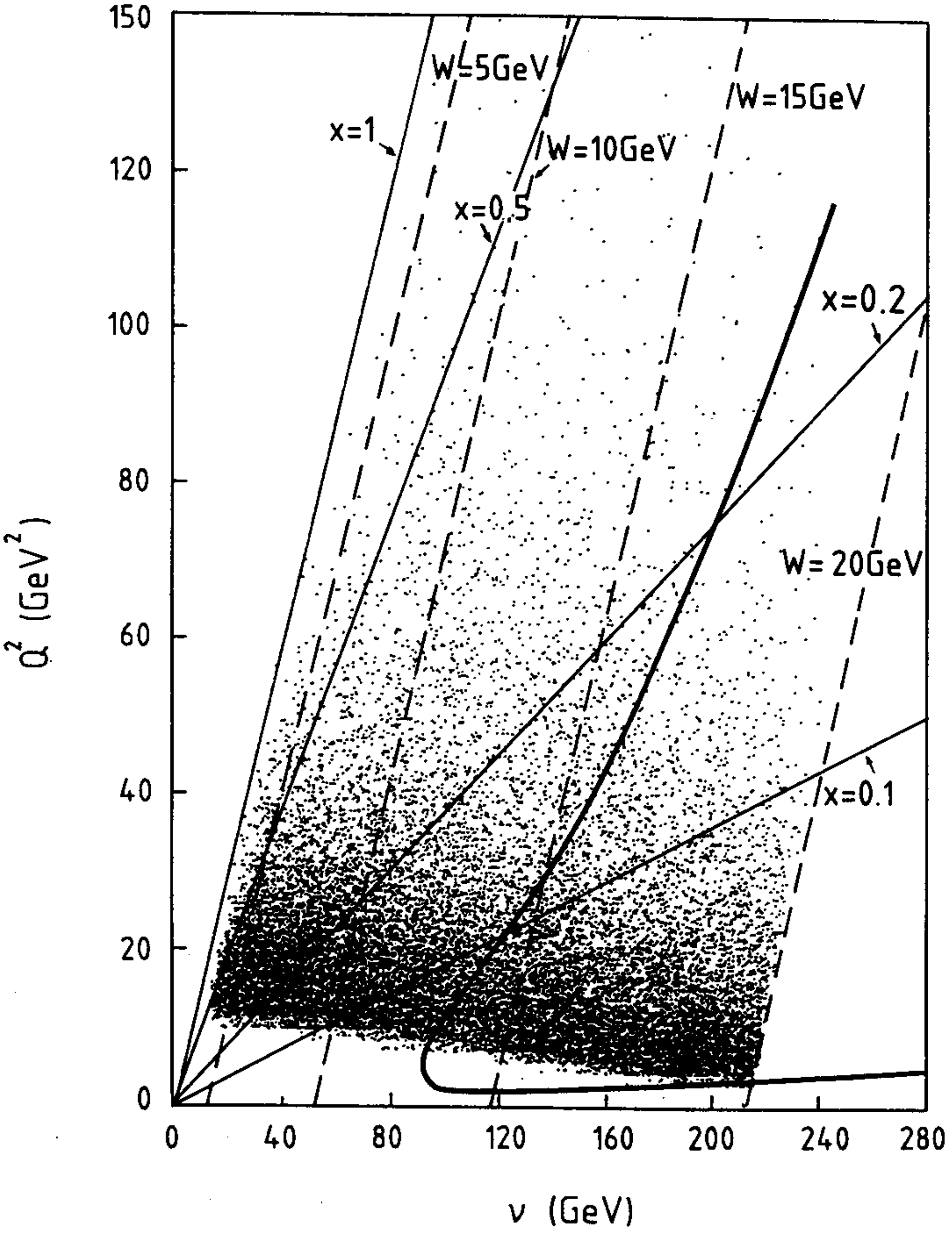
150
120
100
80
60
40
20
0
Q^2 (GeV^2)
0
40
80
120
160
200
240
280
ν (GeV)
x=1
W=5GeV
x=0.5
W=10GeV
W=15GeV
x=0.2
W= 20GeV
x=0.1

FIG. 4

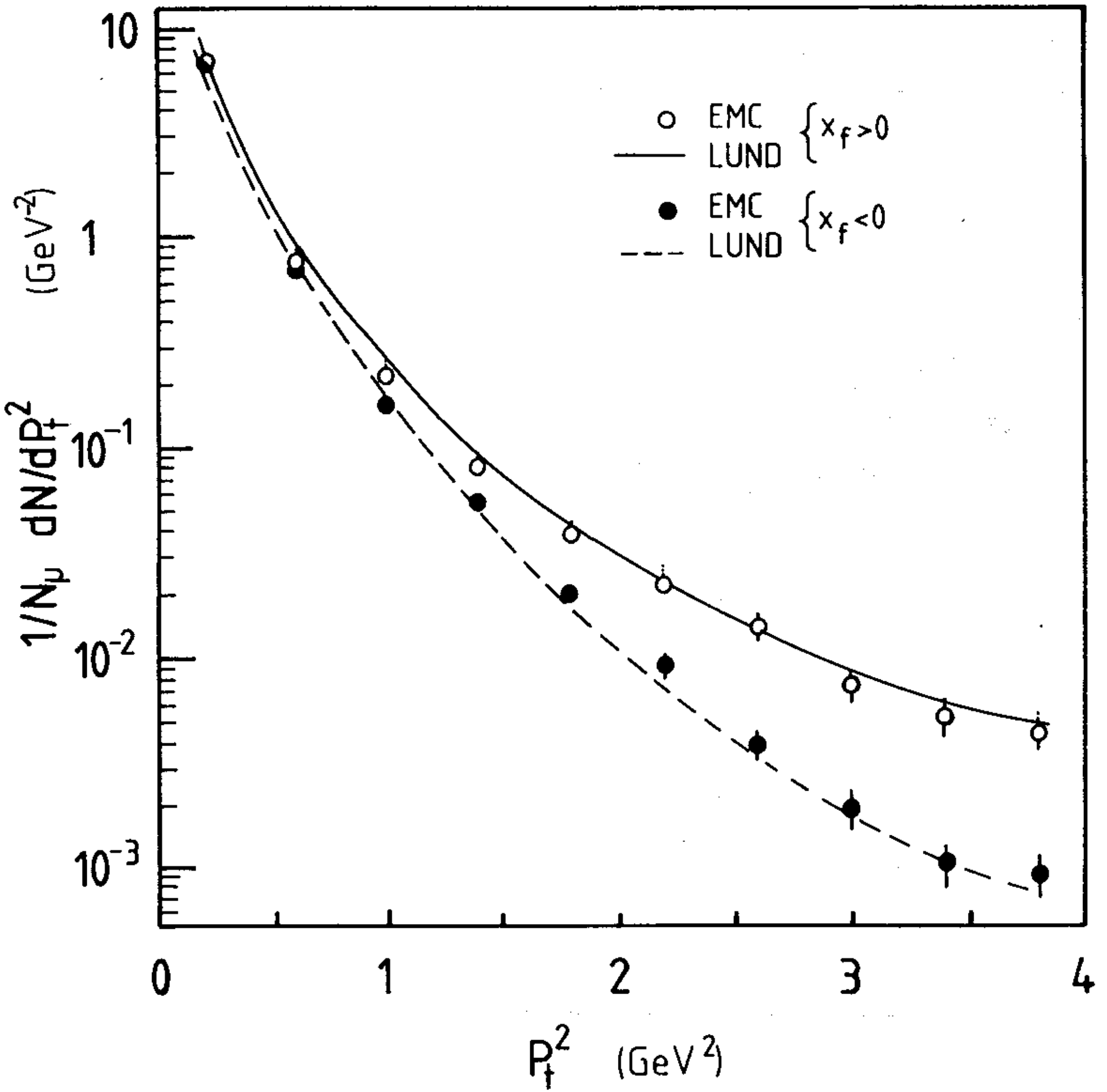

10
1
10^{-1}
10^{-2}
10^{-3}
$1/N_\mu \; dN/dP_t^2$ (GeV^{-2})
0
1
2
3
4
P_t^2 (GeV^2)
EMC
LUND
$\{x_f > 0$
EMC
LUND
$\{x_f < 0$

FIG. 5a

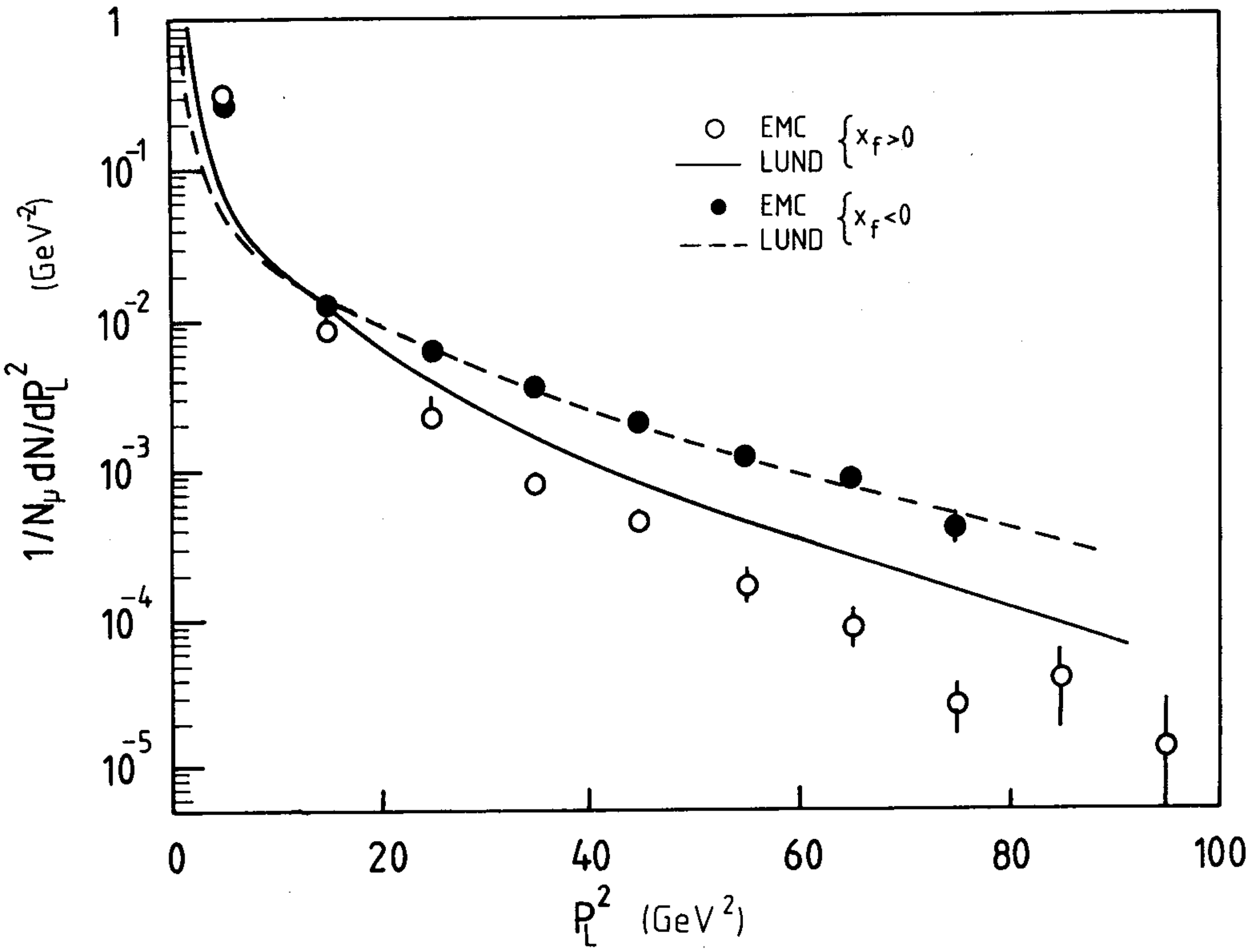
1
10^{-1}
10^{-2}
10^{-3}
10^{-4}
10^{-5}
$1/N_\mu \, dN/dP_L^2$ (GeV^{-2})
0
20
40
60
80
100
P_L^2 (GeV^2)
EMC
LUND
$\{x_f > 0$
EMC
LUND
$\{x_f < 0$

FIG. 5b

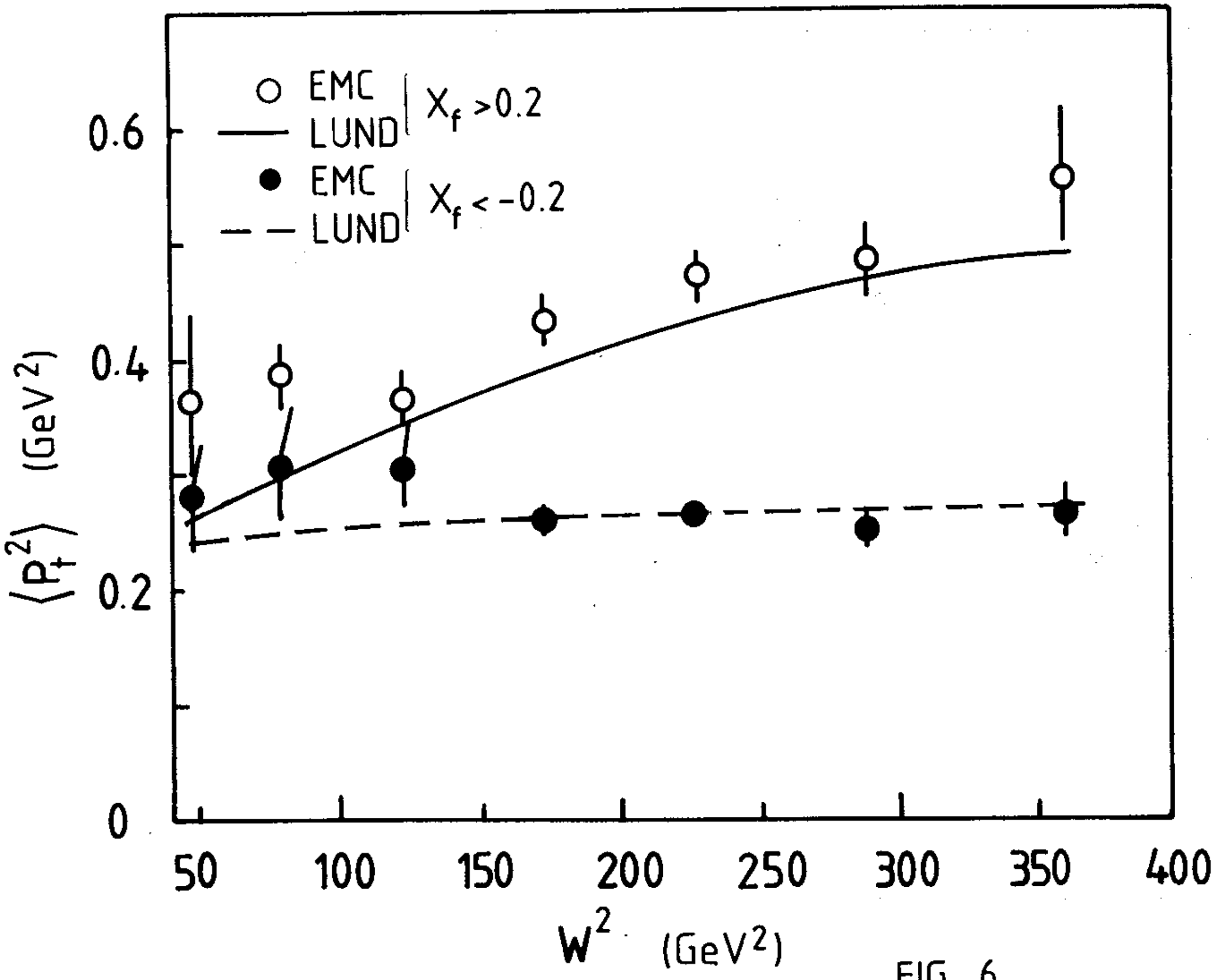
EMC
LUND
EMC
LUND
$X_f > 0.2$
$X_f < -0.2$
0.6
0.4
0.2
0
$\langle P_t^2 \rangle$ (GeV^2)
50
100
150
200
250
300
350
400
W^2 (GeV^2)

FIG. 6

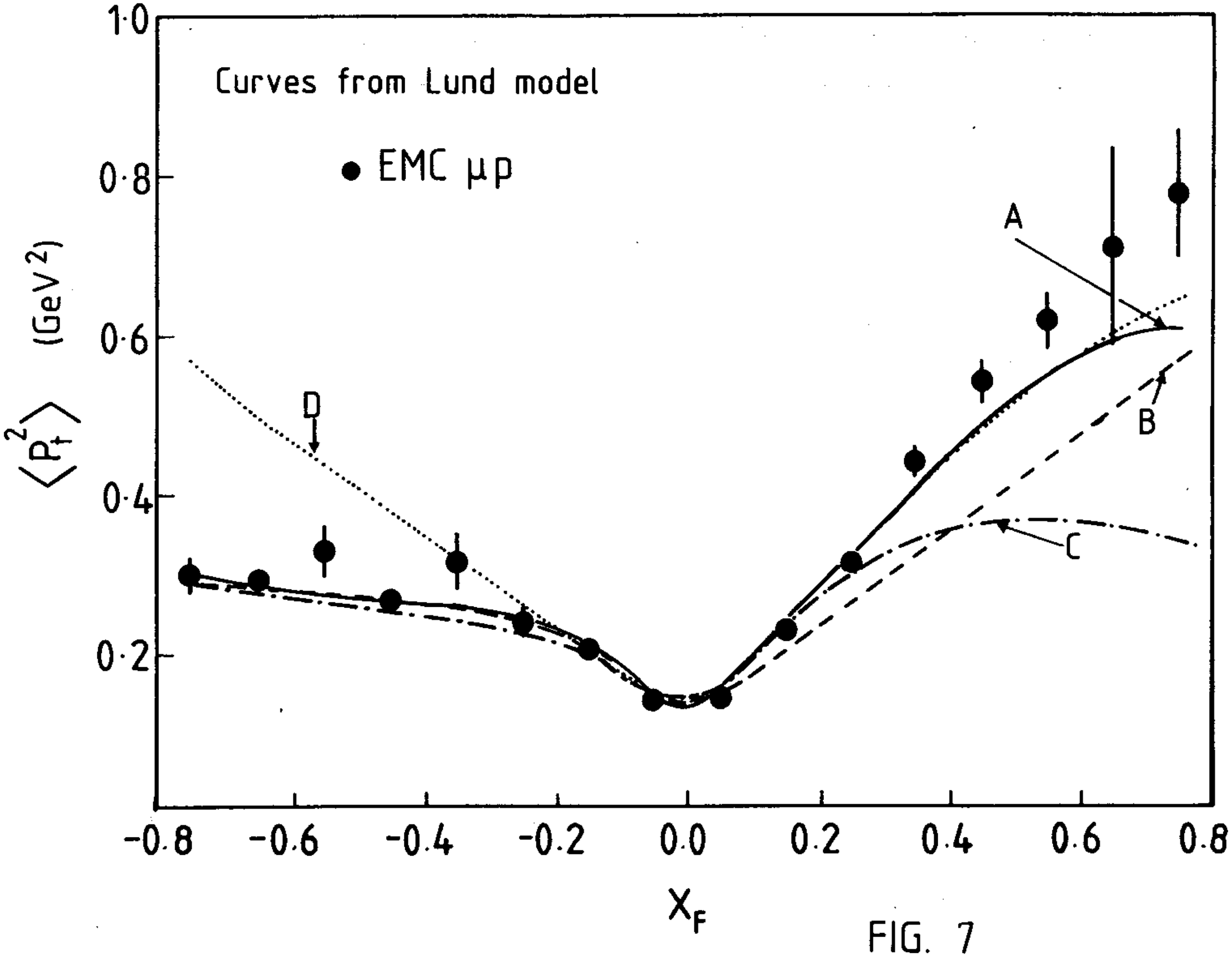
Curves from Lund model
● EMC μp
A
B
C
D
$\langle P_t^2 \rangle$ (GeV^2)
1·0
0·8
0·6
0·4
0·2
X_F
-0.8
-0.6
-0.4
-0.2
0.0
0.2
0.4
0.6
0.8

FIG. 7

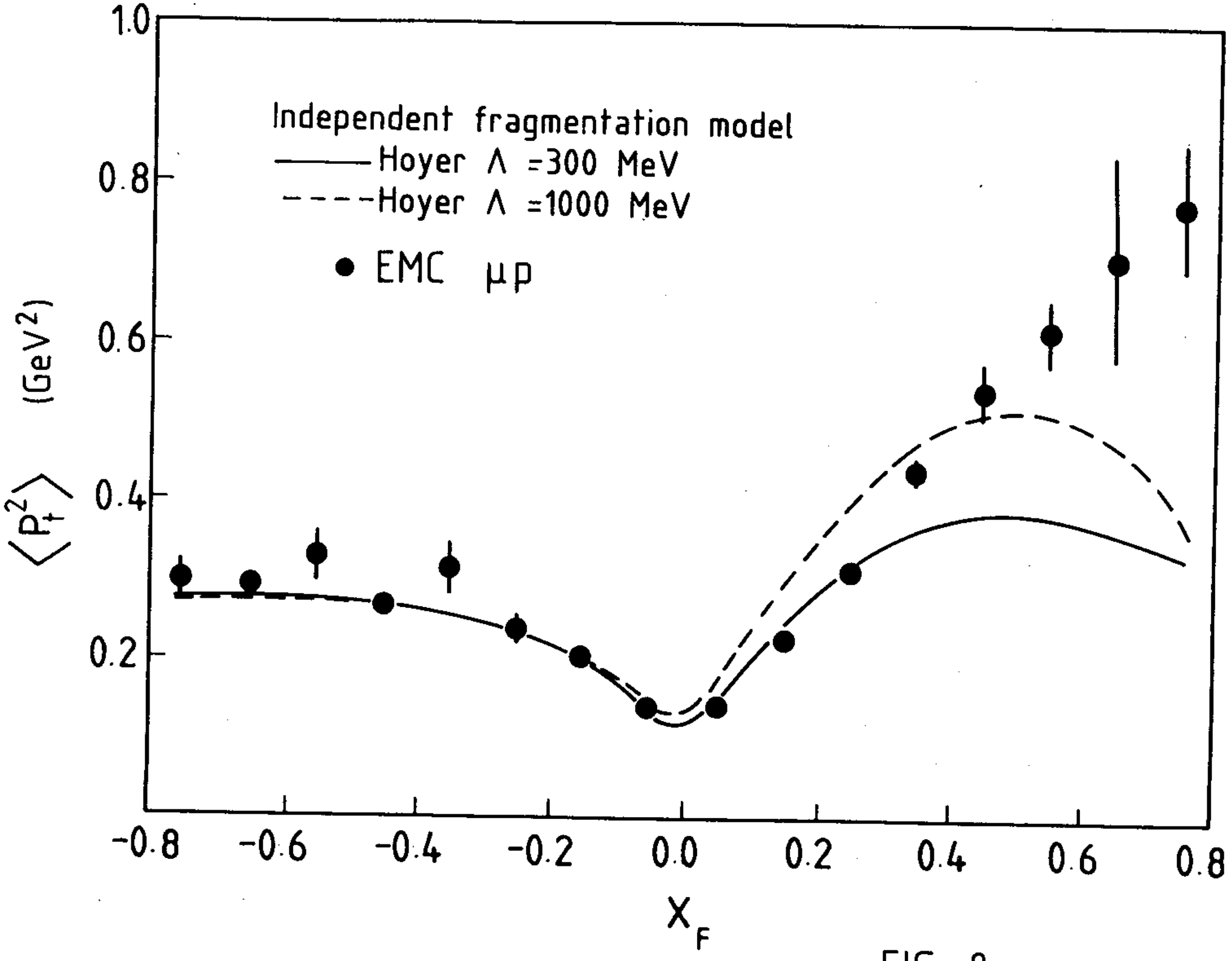
Independent fragmentation model
——Hoyer Λ =300 MeV
----Hoyer Λ =1000 MeV
● EMC μp
$\langle P_t^2 \rangle$ (GeV^2)
1.0
0.8
0.6
0.4
0.2
−0.8
−0.6
−0.4
−0.2
0.0
0.2
0.4
0.6
0.8
X_F

FIG. 8

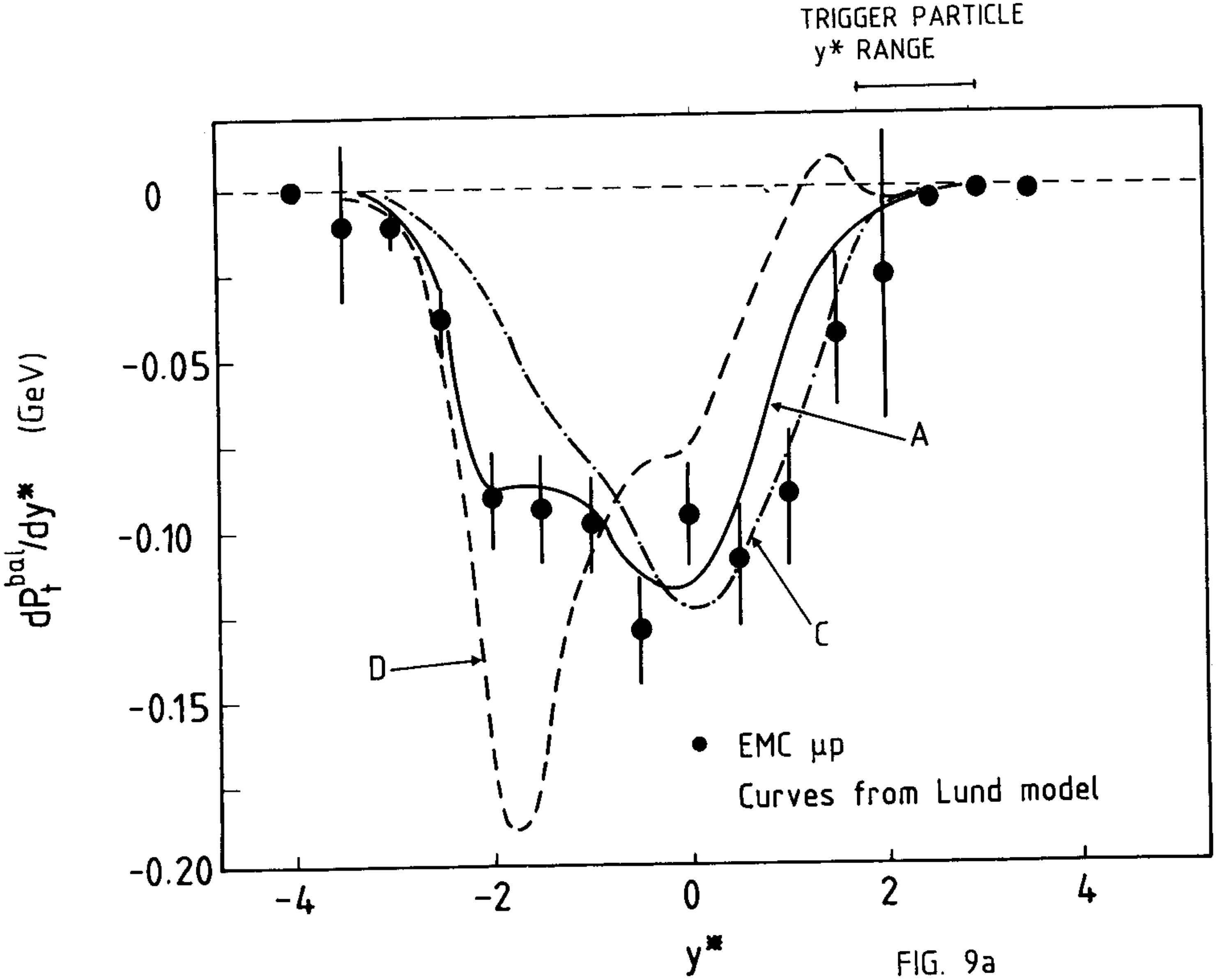
TRIGGER PARTICLE
y* RANGE
0
-0.05
-0.10
-0.15
-0.20
dP_t^{bal}/dy^* (GeV)
-4
-2
0
2
4
y^*
A
C
D
● EMC μp
Curves from Lund model

FIG. 9a

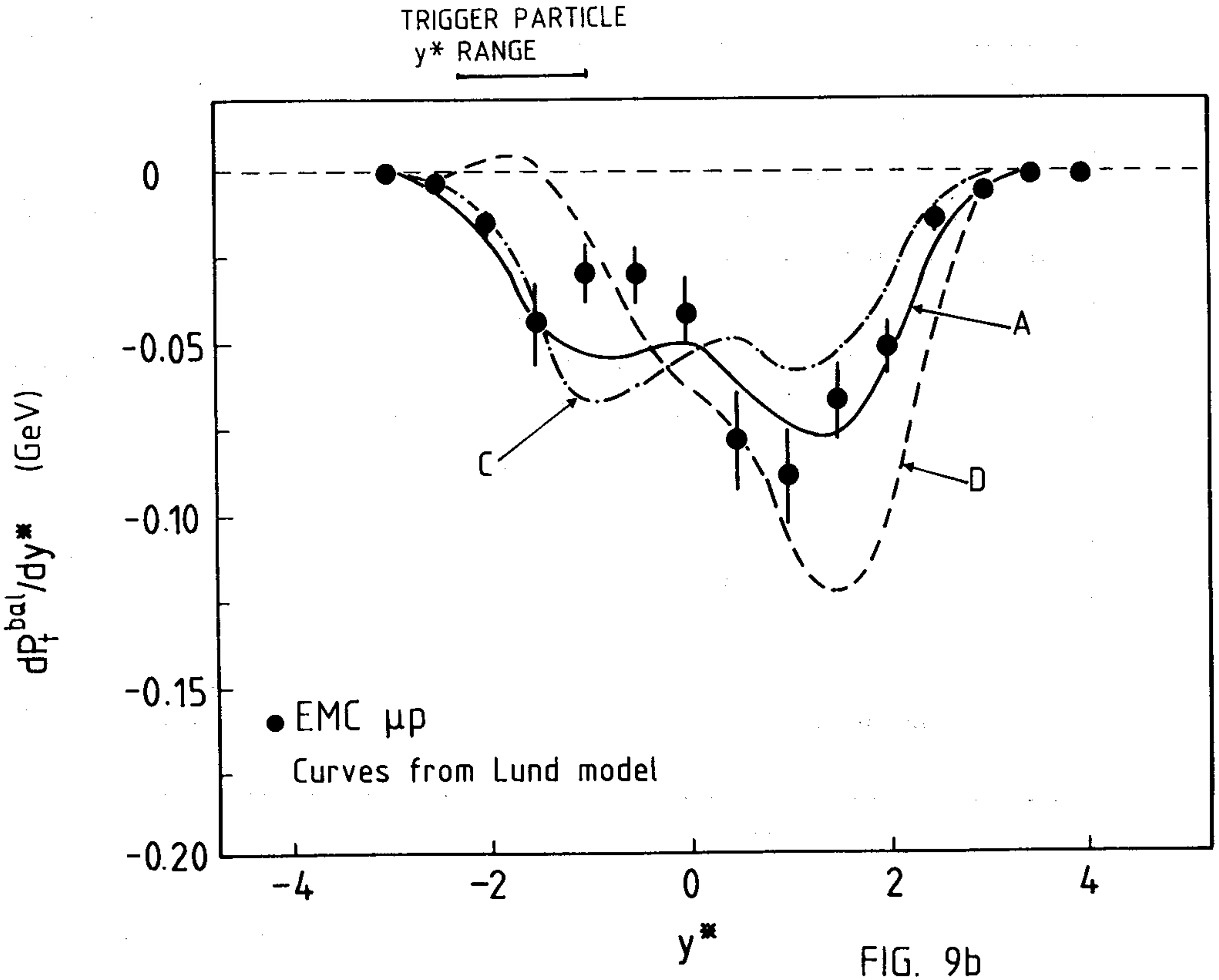
TRIGGER PARTICLE
y* RANGE
0
-0.05
-0.10
-0.15
-0.20
dP_t^{bal}/dy^* (GeV)
-4
-2
0
2
4
y*
A
C
D
● EMC μp
Curves from Lund model

FIG. 9b

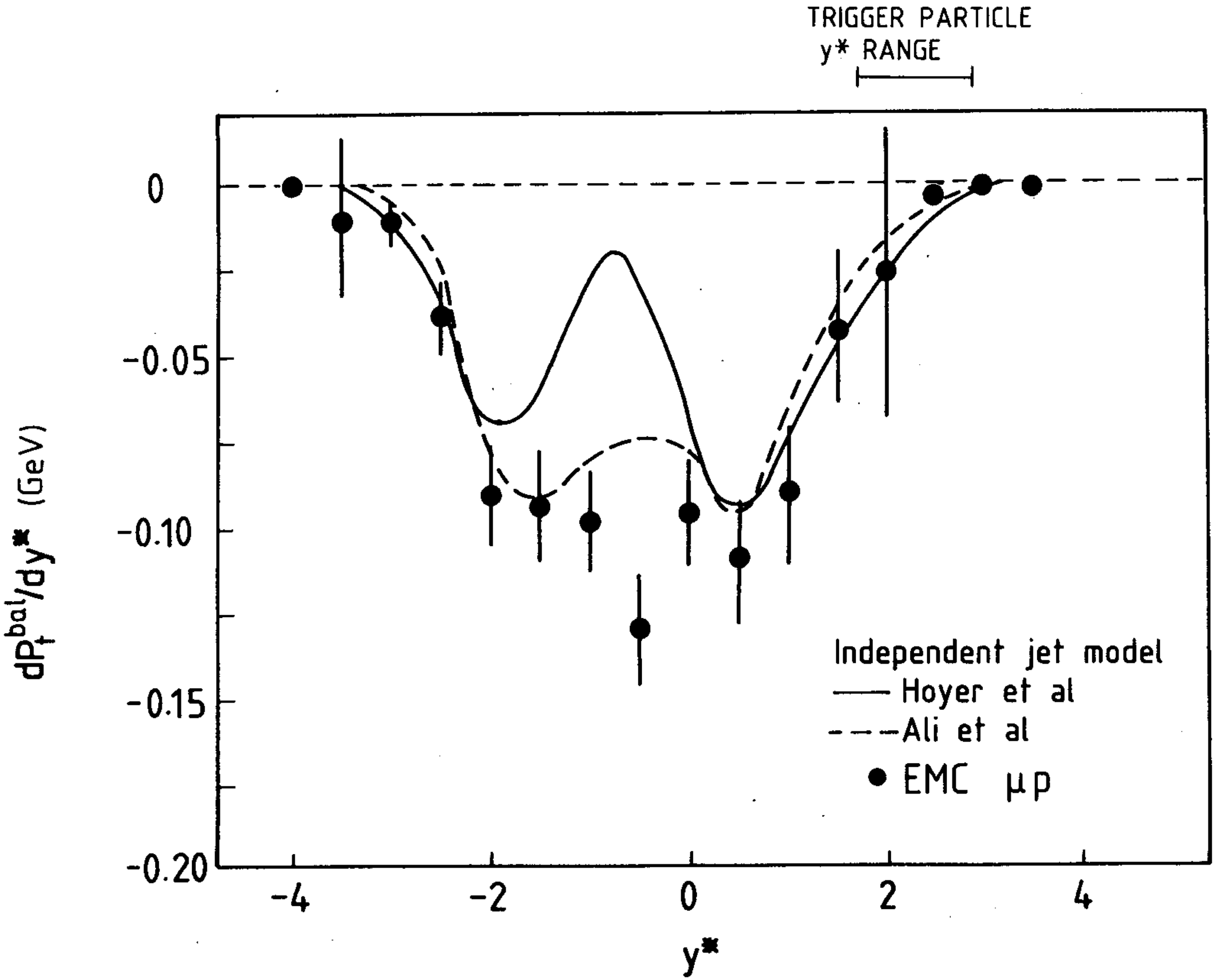
TRIGGER PARTICLE
y* RANGE
0
-0.05
-0.10
-0.15
-0.20
dP_t^{bal}/dy^* (GeV)
-4
-2
0
2
4
y*
Independent jet model
—— Hoyer et al
- - - Ali et al
● EMC μp

FIG. 10a

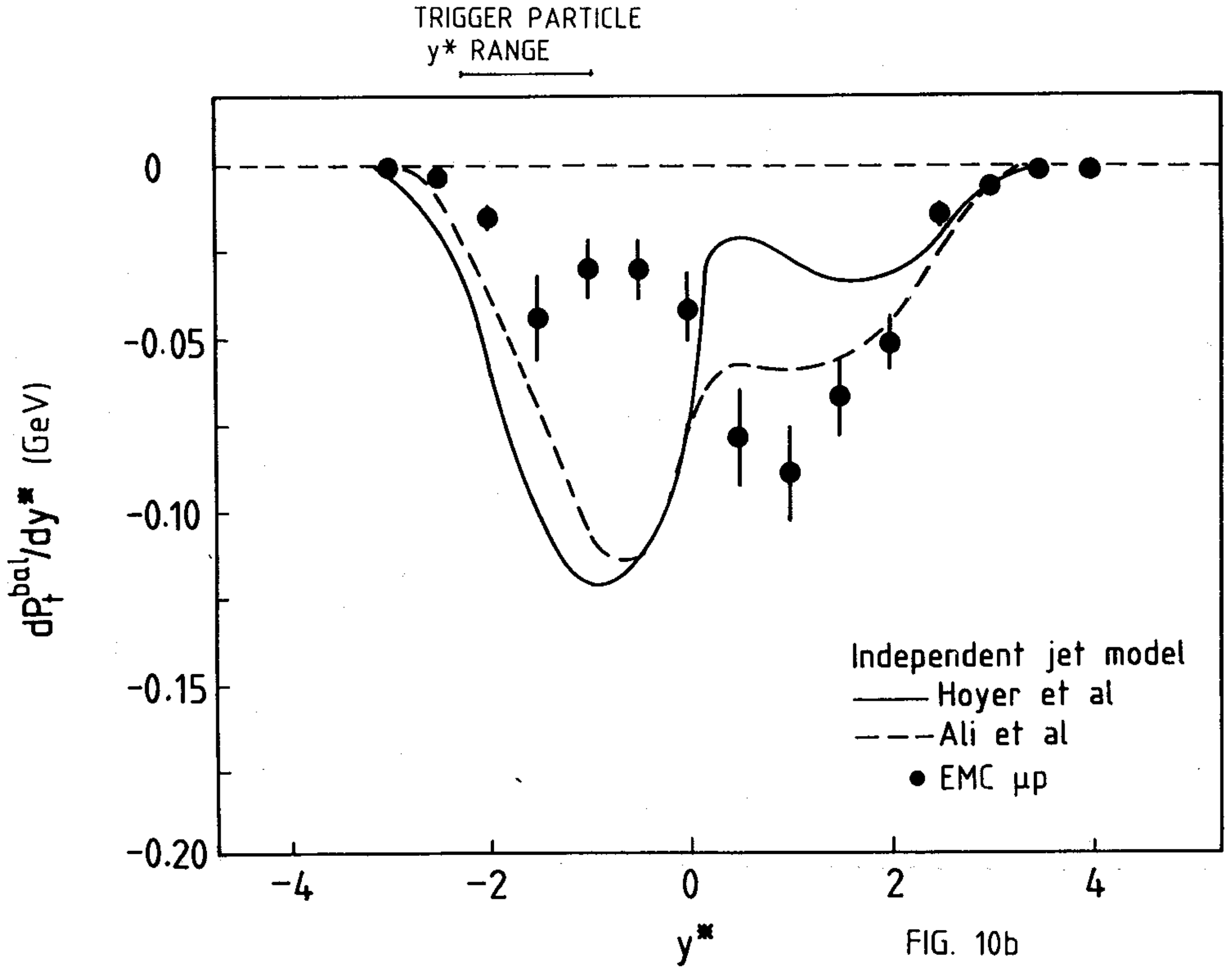
TRIGGER PARTICLE
y* RANGE
0
-0.05
-0.10
-0.15
-0.20
dP_t^{bal}/dy^* (GeV)
-4
-2
0
2
4
y*
Independent jet model
Hoyer et al
Ali et al
● EMC μp

FIG. 10b

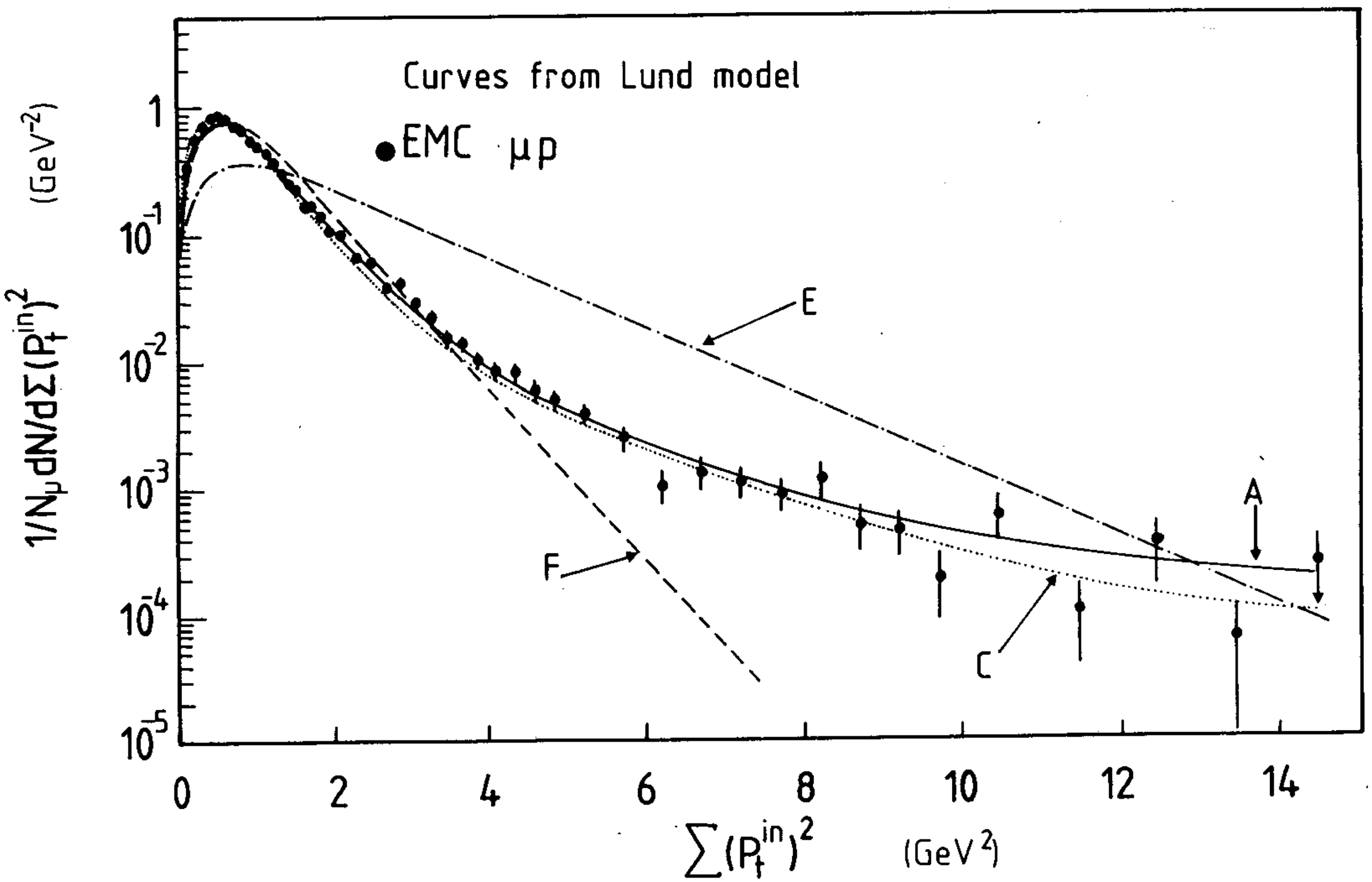
Curves from Lund model
● EMC μp
$1/N_\mu \, dN/d\Sigma(P_t^{in})^2$ (GeV^{-2})
1
10^{-1}
10^{-2}
10^{-3}
10^{-4}
10^{-5}
0
2
4
6
8
10
12
14
$\sum(P_t^{in})^2$ (GeV^2)
E
F
A
C

FIG. 11a

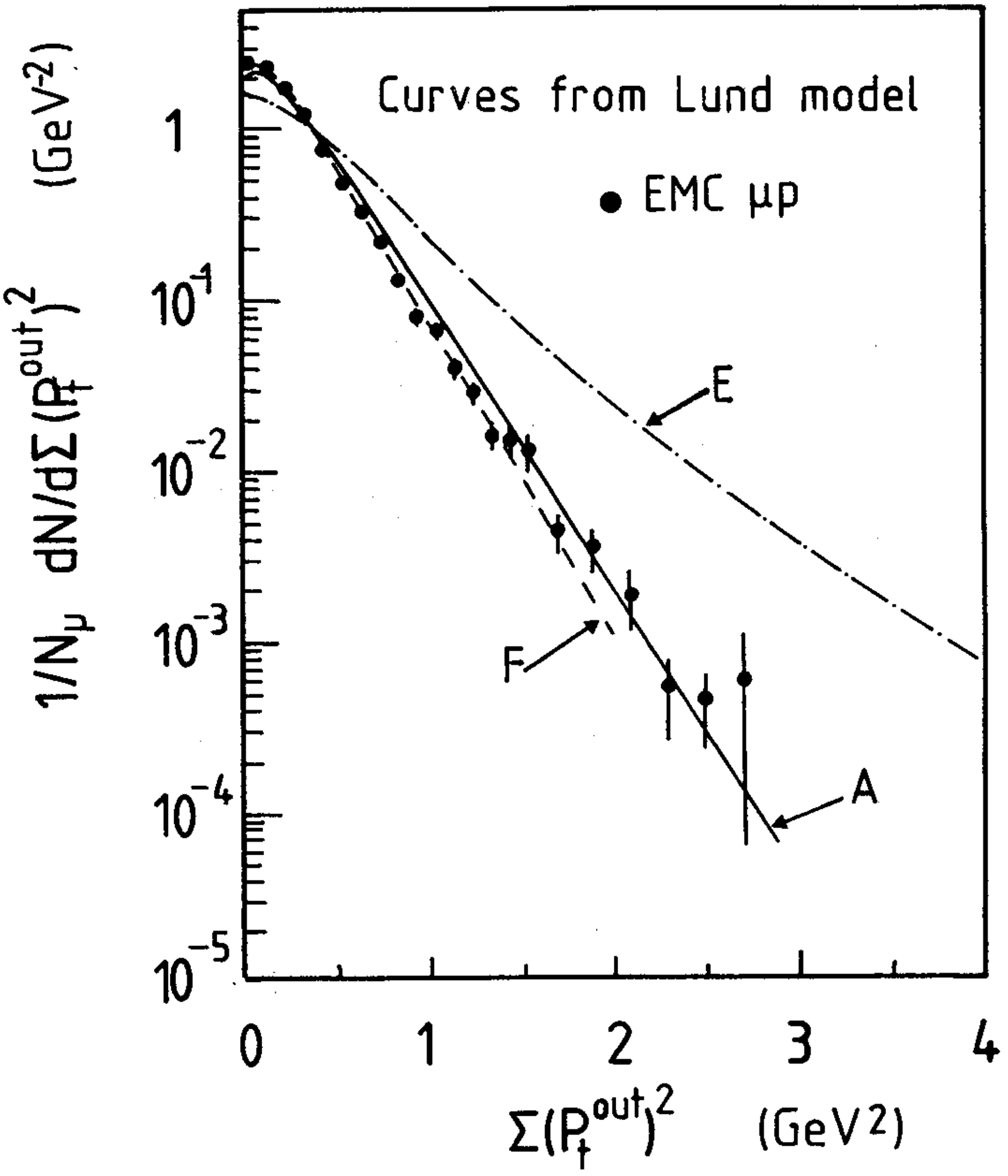
Curves from Lund model
● EMC μp
E
F
A
$1/N_\mu \; dN/d\Sigma(P_t^{out})^2 \; (GeV^{-2})$
1
10^{-1}
10^{-2}
10^{-3}
10^{-4}
10^{-5}
0
1
2
3
4
$\Sigma(P_t^{out})^2 \; (GeV^2)$

FIG. 11b

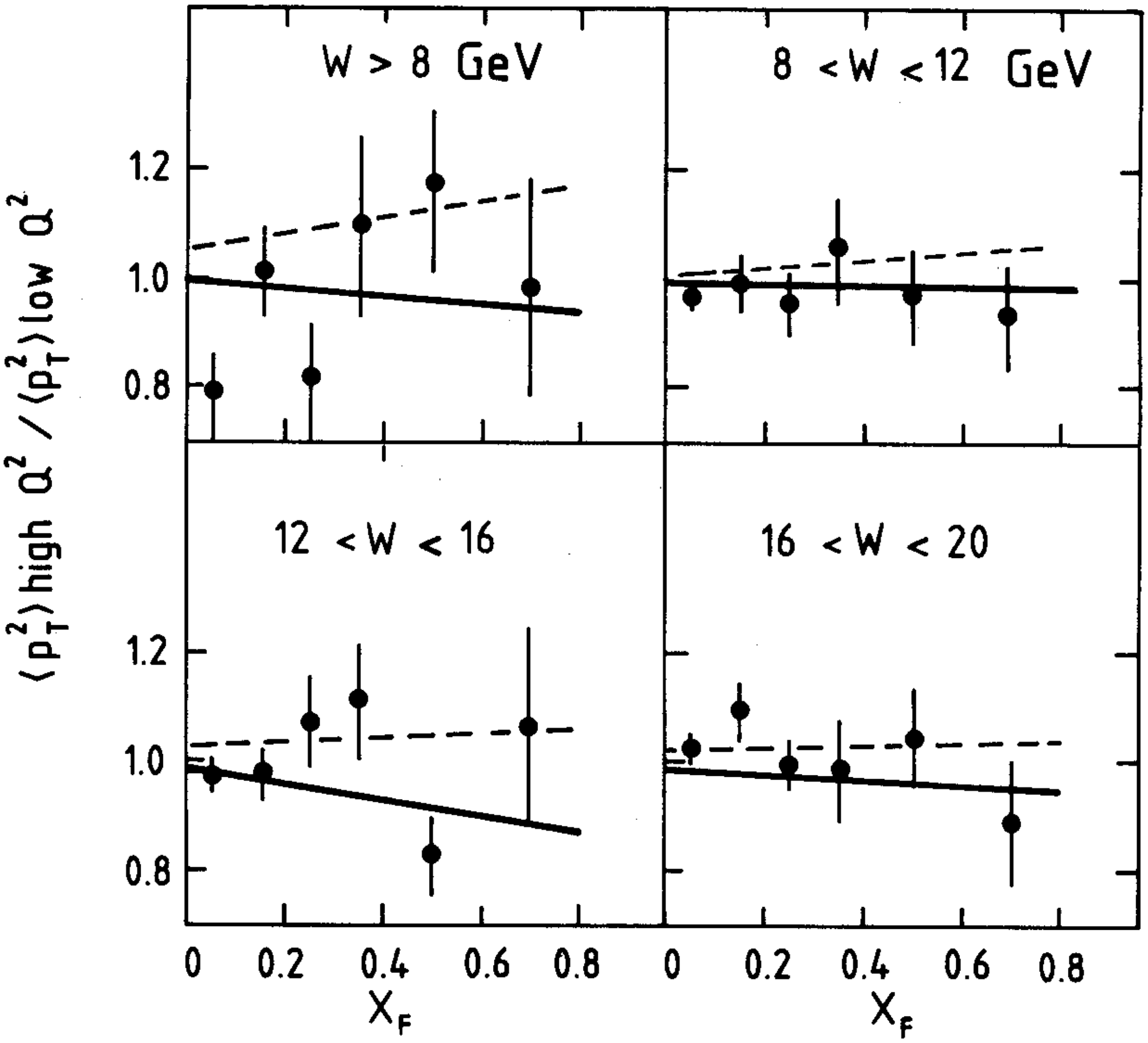
W > 8 GeV
8 < W < 12 GeV
12 < W < 16
16 < W < 20
1.2
1.0
0.8
⟨p_T^2⟩ high Q^2 / ⟨p_T^2⟩ low Q^2
0
0.2
0.4
0.6
0.8
X_F

FIG. 12

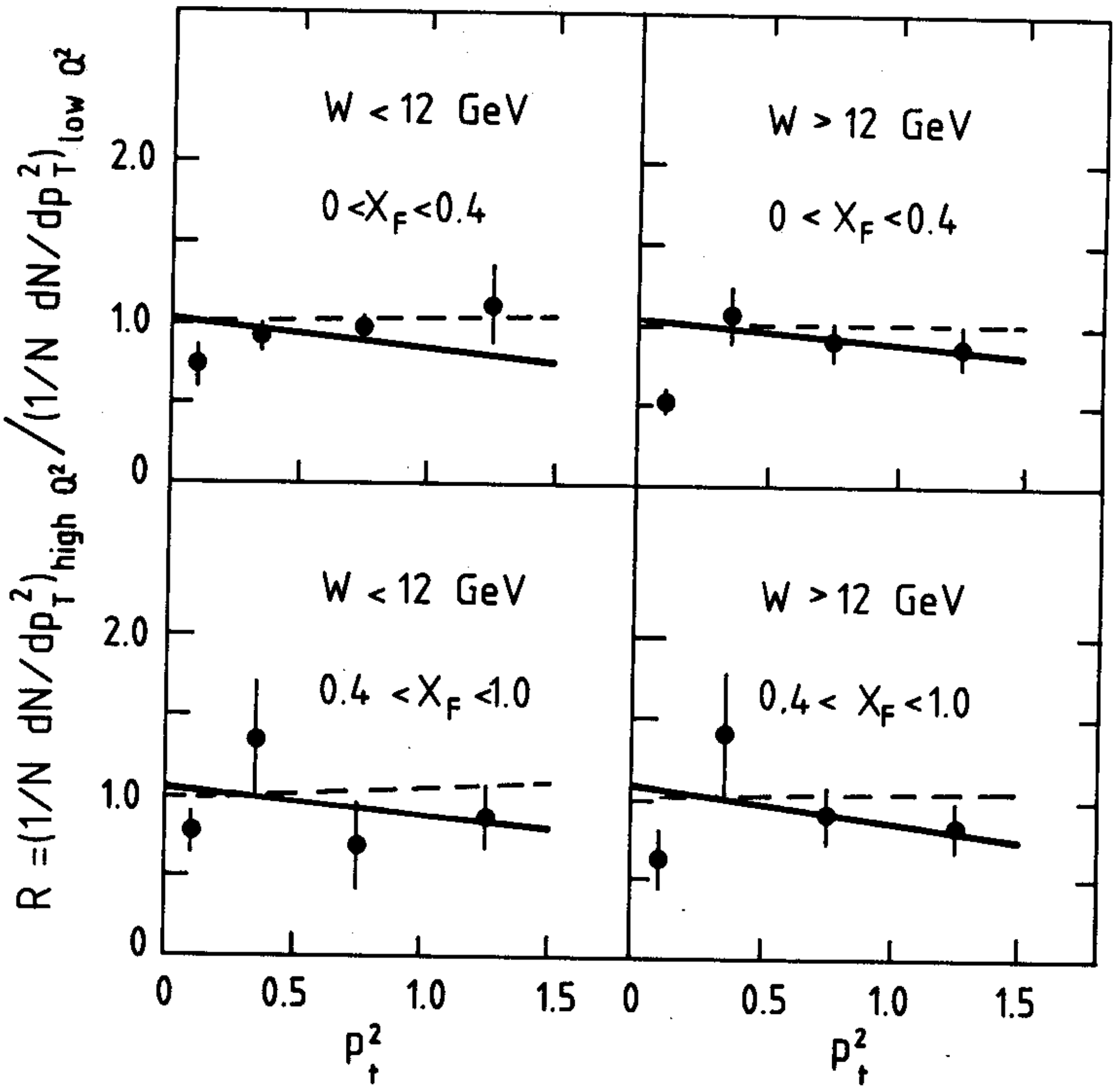
W < 12 GeV
0 < X_F < 0.4
W > 12 GeV
0 < X_F < 0.4
W < 12 GeV
0.4 < X_F < 1.0
W > 12 GeV
0.4 < X_F < 1.0
$R = (1/N\ dN/dp_T^2)_{\text{high } Q^2} / (1/N\ dN/dp_T^2)_{\text{low } Q^2}$
0
1.0
2.0
0
0.5
1.0
1.5
p_t^2

FIG. 13

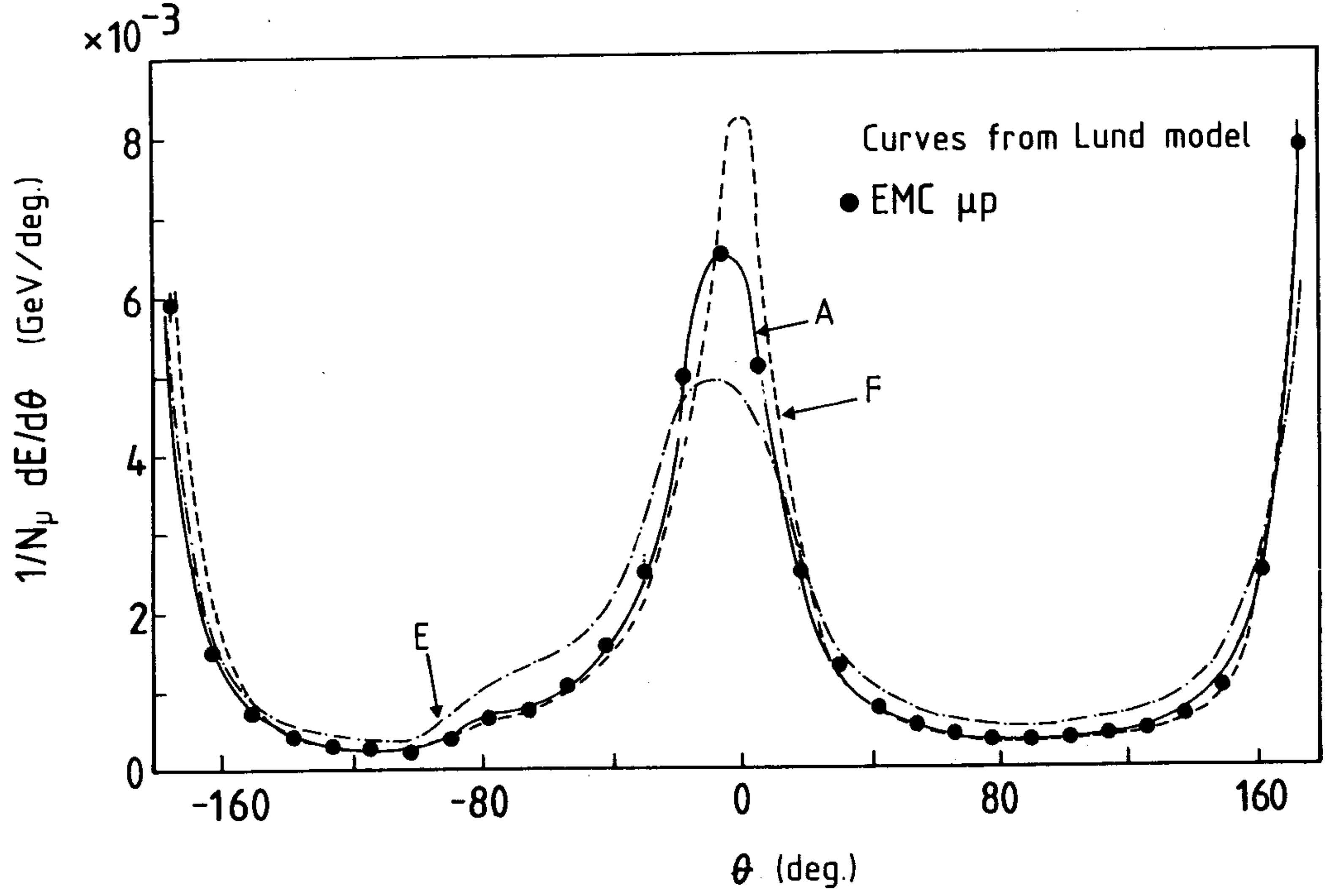
×10^{-3}
Curves from Lund model
● EMC μp
A
F
E
1/N$_\mu$ dE/dθ (GeV/deg.)
0
2
4
6
8
-160
-80
0
80
160
θ (deg.)

FIG. 14

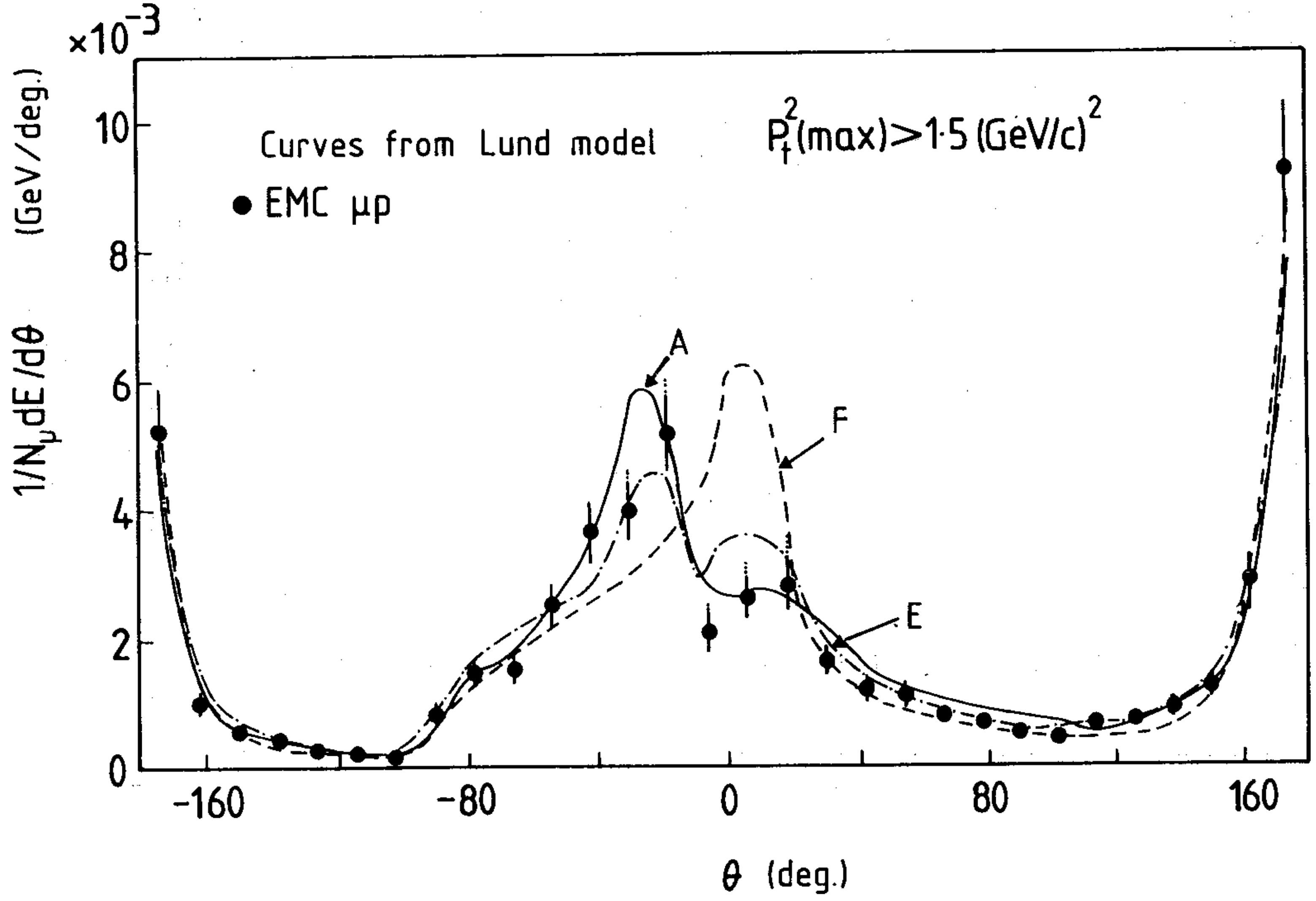×10^{-3}
(GeV/deg.)
1/N$_\mu$ dE/dθ
10
8
6
4
2
0
Curves from Lund model
P_t^2(max)>1·5 (GeV/c)^2
● EMC μp
A
F
E
-160
-80
0
80
160
θ (deg.)

FIG. 15

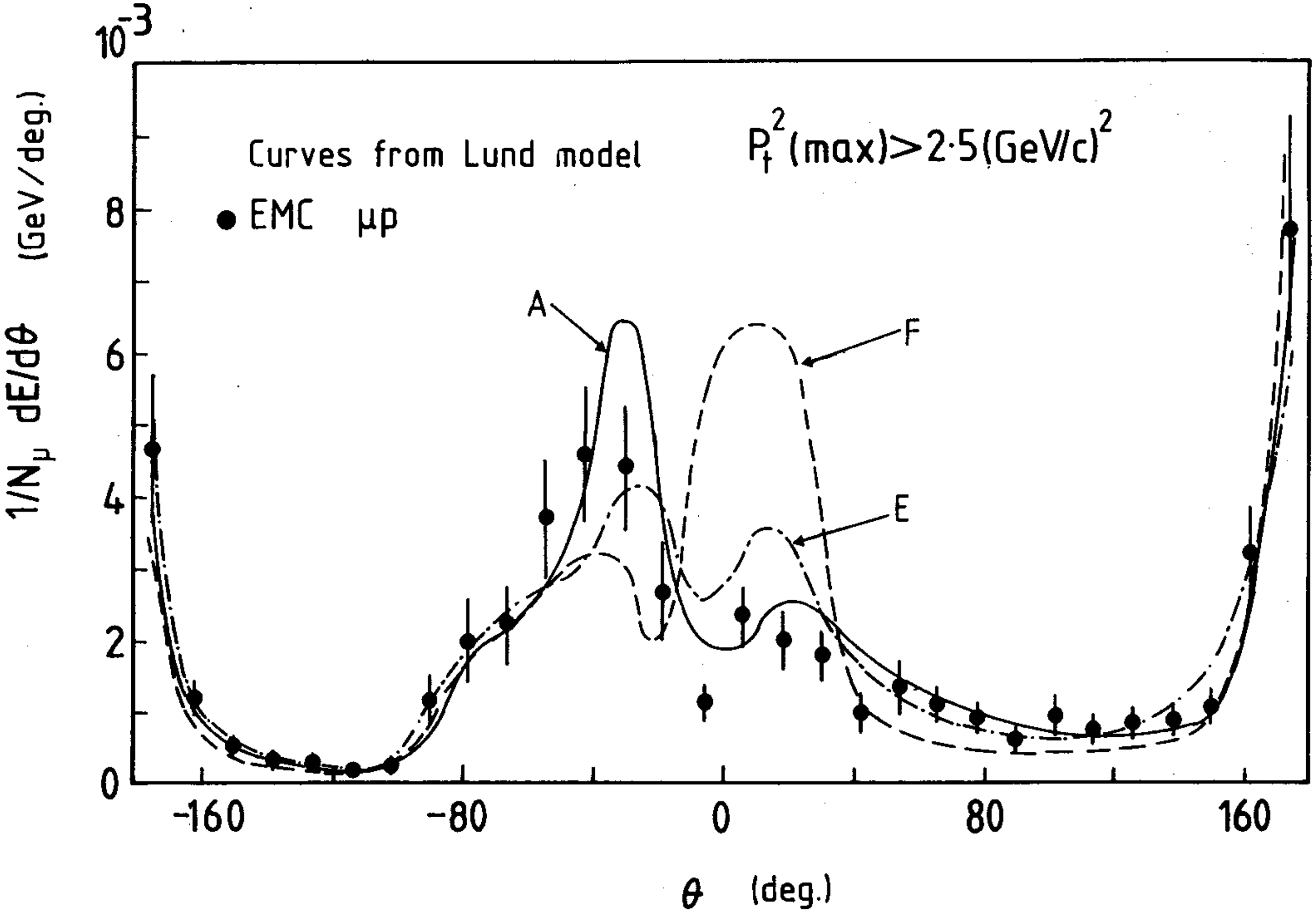
10^{-3}
Curves from Lund model
$P_t^2(\max) > 2{\cdot}5\,(\mathrm{GeV/c})^2$
● EMC μp
A
F
E
$1/N_\mu\ dE/d\theta$ (GeV/deg.)
0
2
4
6
8
-160
-80
0
80
160
θ (deg.)

FIG. 16

FORWARD

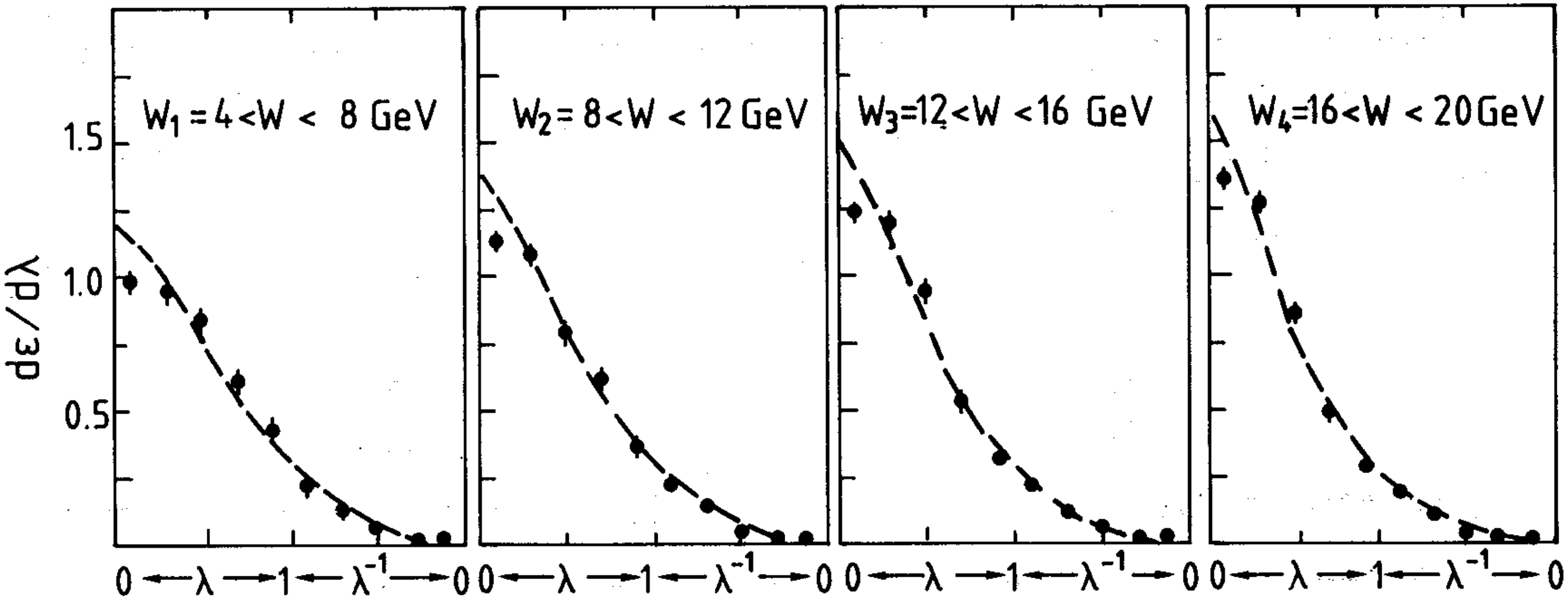

FIG. 17a

BACKWARD

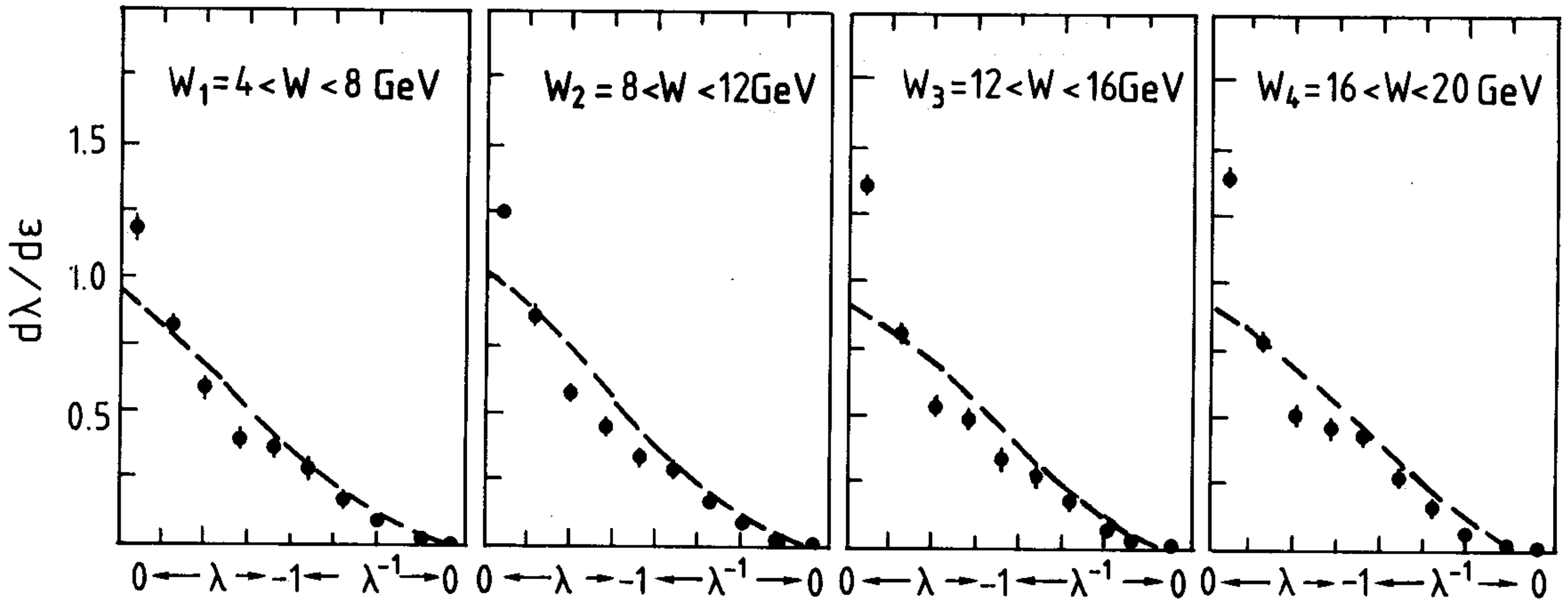

FIG. 17b

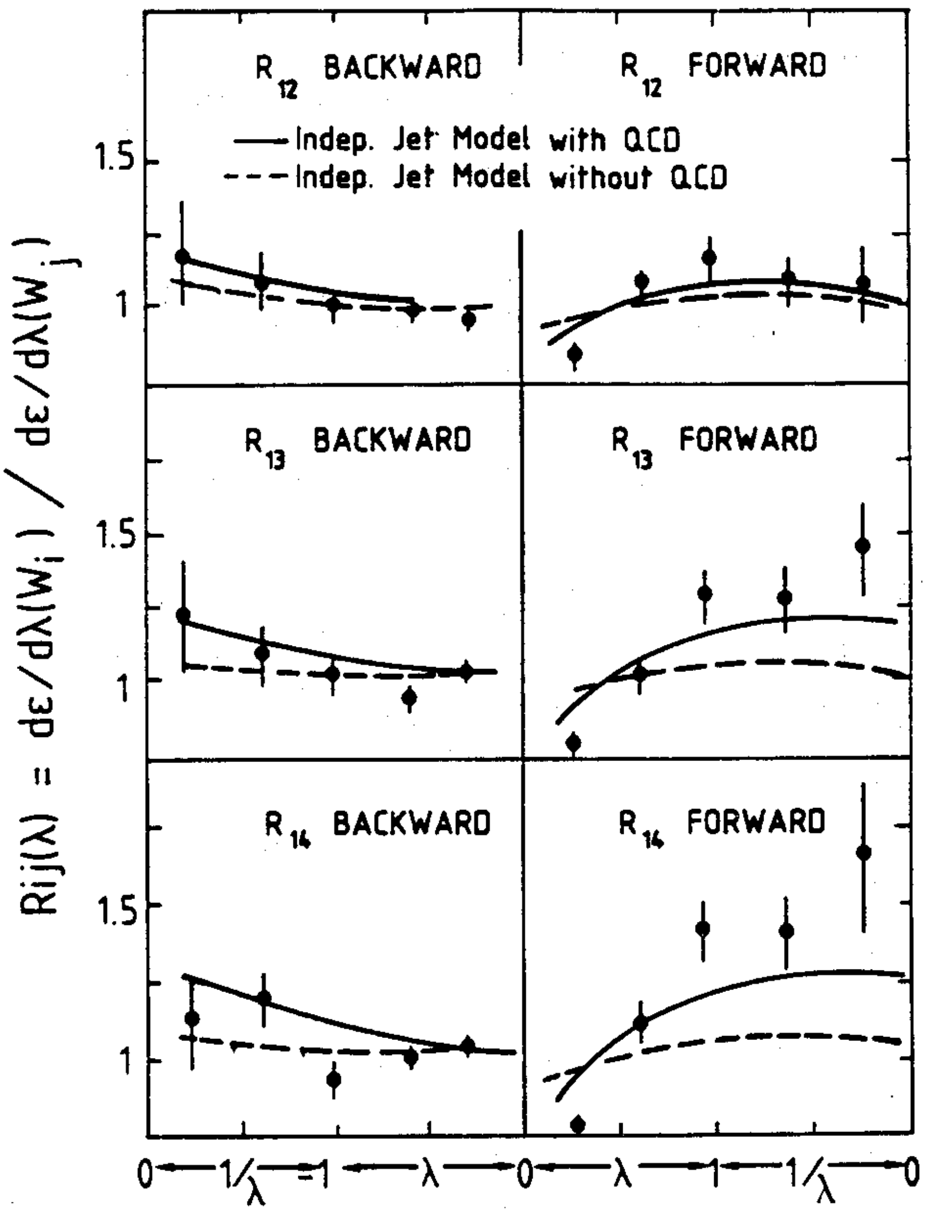
R_{12} BACKWARD
R_{12} FORWARD
—— Indep. Jet Model with QCD
- - - Indep. Jet Model without QCD
R_{13} BACKWARD
R_{13} FORWARD
R_{14} BACKWARD
R_{14} FORWARD
1.5
1
$Rij(\lambda) = d\varepsilon/d\lambda(W_i) \;/\; d\varepsilon/d\lambda(W_j)$
0 ← 1/λ → 1 ← λ → 0 ← λ → 1 ← 1/λ → 0

FIG. 18

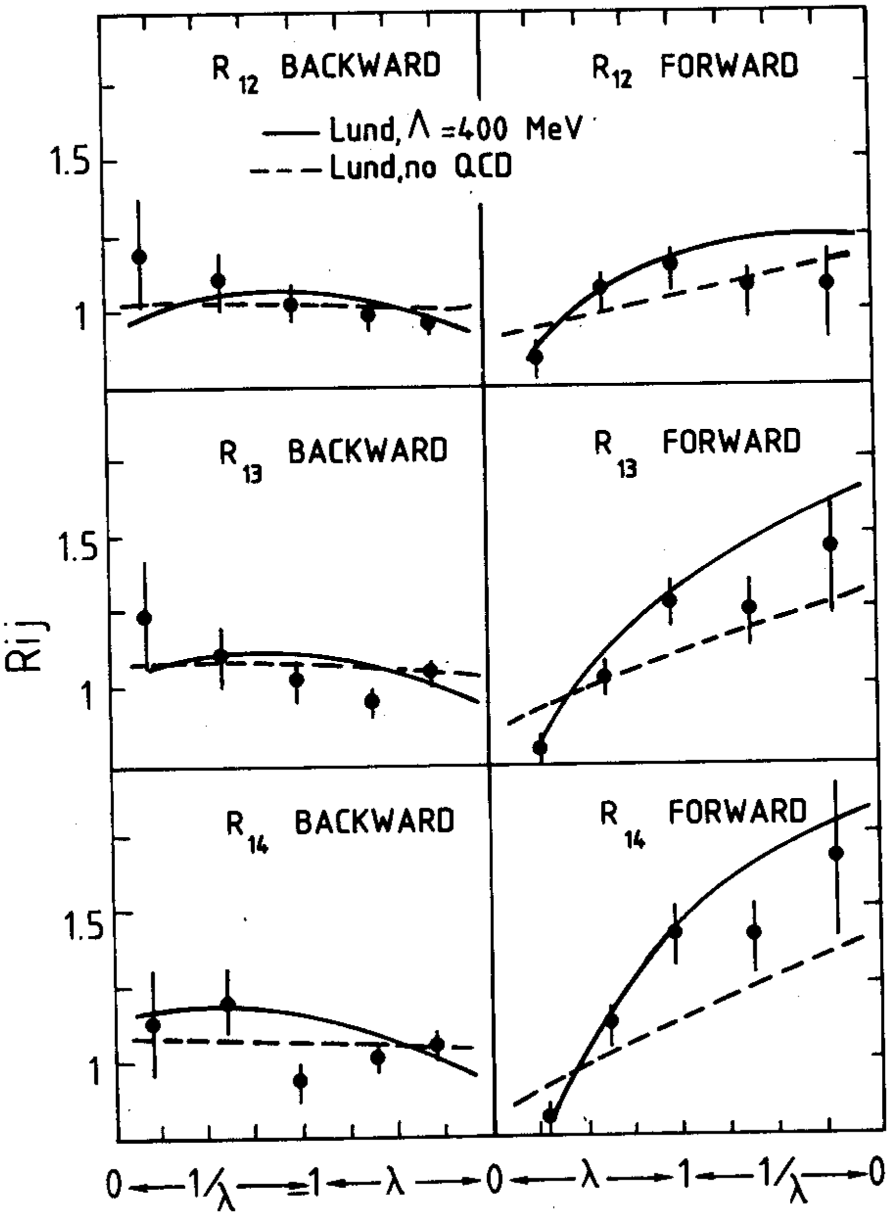
R12 BACKWARD
R12 FORWARD
Lund, Λ =400 MeV
Lund, no QCD
R13 BACKWARD
R13 FORWARD
R14 BACKWARD
R14 FORWARD
Rij
1.5
1
1.5
1
1.5
1
0 ← 1/λ → 1 ← λ → 0 ← λ → 1 ← 1/λ → 0

FIG. 19

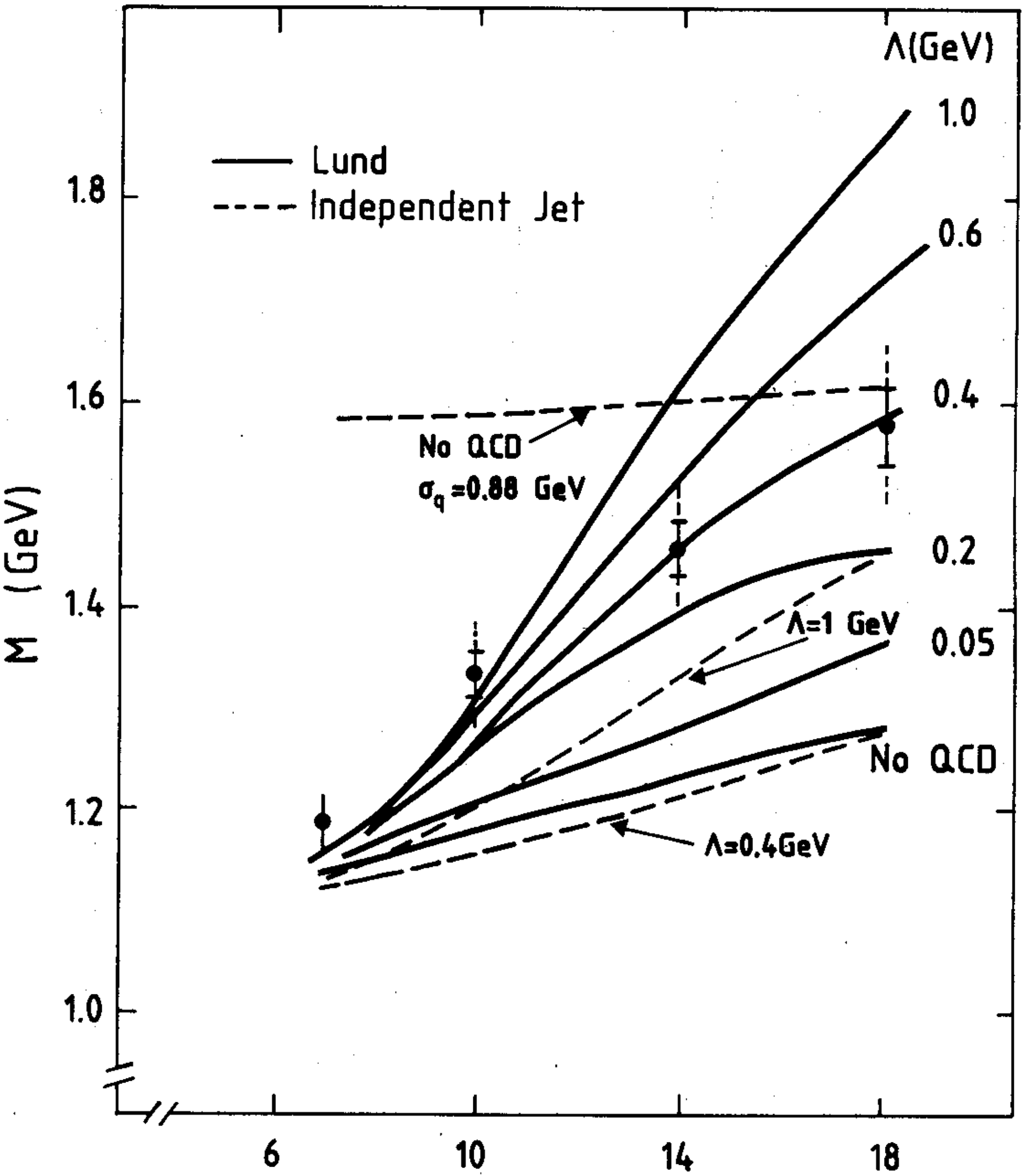
Λ(GeV)
1.0
0.6
0.4
0.2
0.05
No QCD
Lund
Independent Jet
No QCD
σ_q =0.88 GeV
Λ=1 GeV
Λ=0.4GeV
M (GeV)
1.0
1.2
1.4
1.6
1.8
6
10
14
18
W(GeV)

FIG. 20

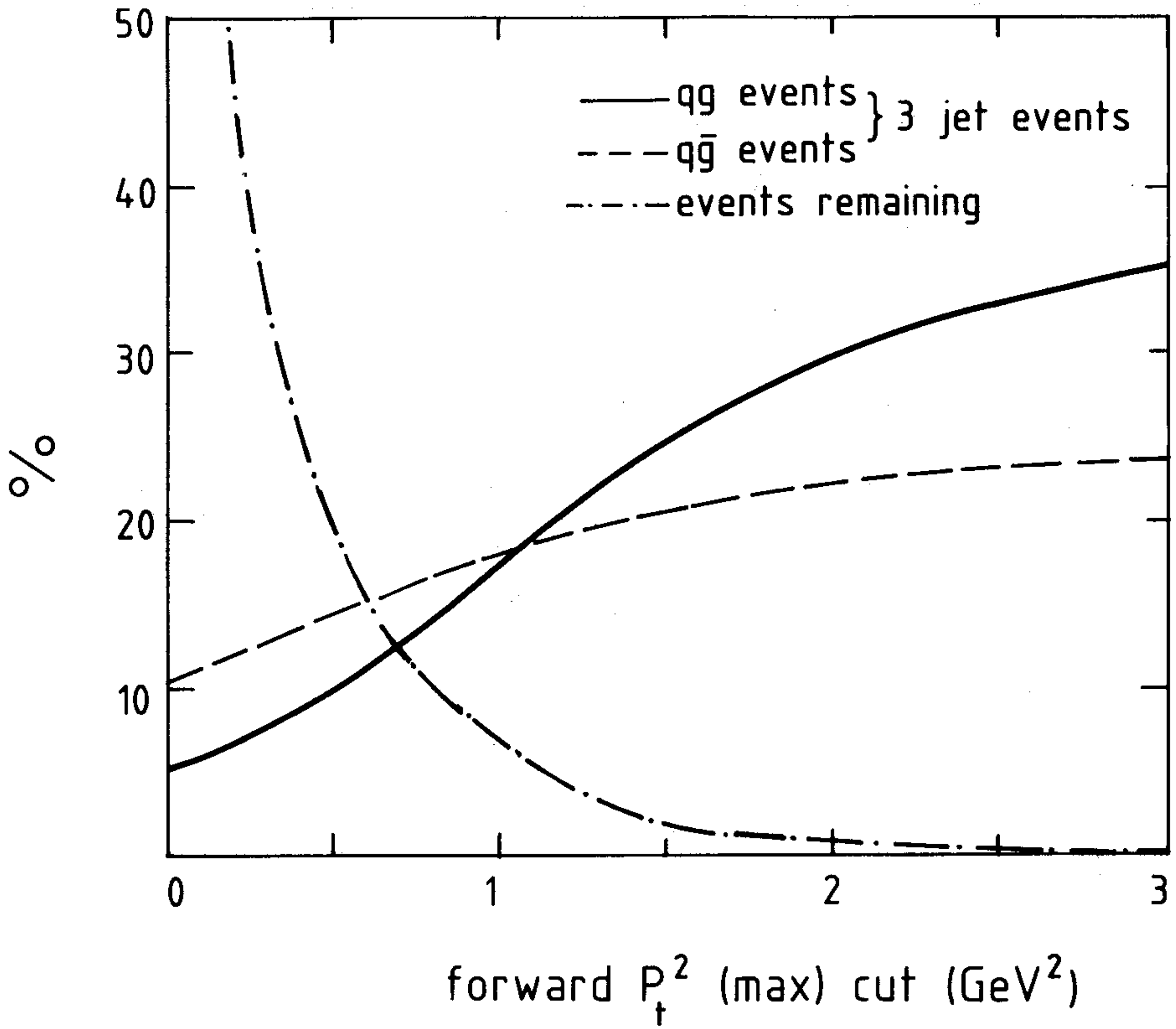

qg events
$q\bar{g}$ events
} 3 jet events
events remaining
%
50
40
30
20
10
0
1
2
3
forward P_t^2 (max) cut (GeV^2)

FIG. 21

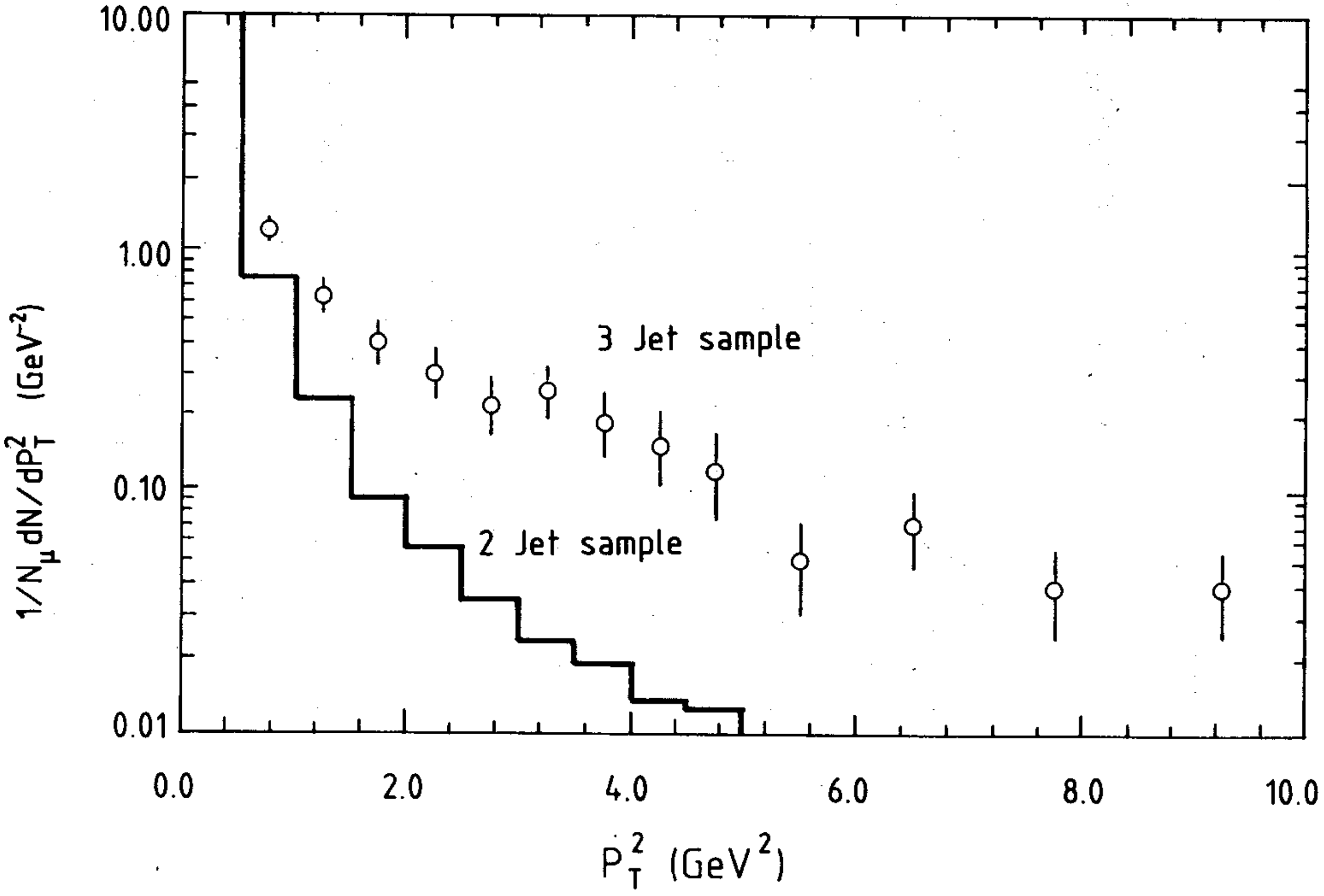
10.00
1.00
0.10
0.01
$1/N_\mu dN/dP_T^2$ (GeV^{-2})
0.0
2.0
4.0
6.0
8.0
10.0
P_T^2 (GeV^2)
3 Jet sample
2 Jet sample

FIG. 22

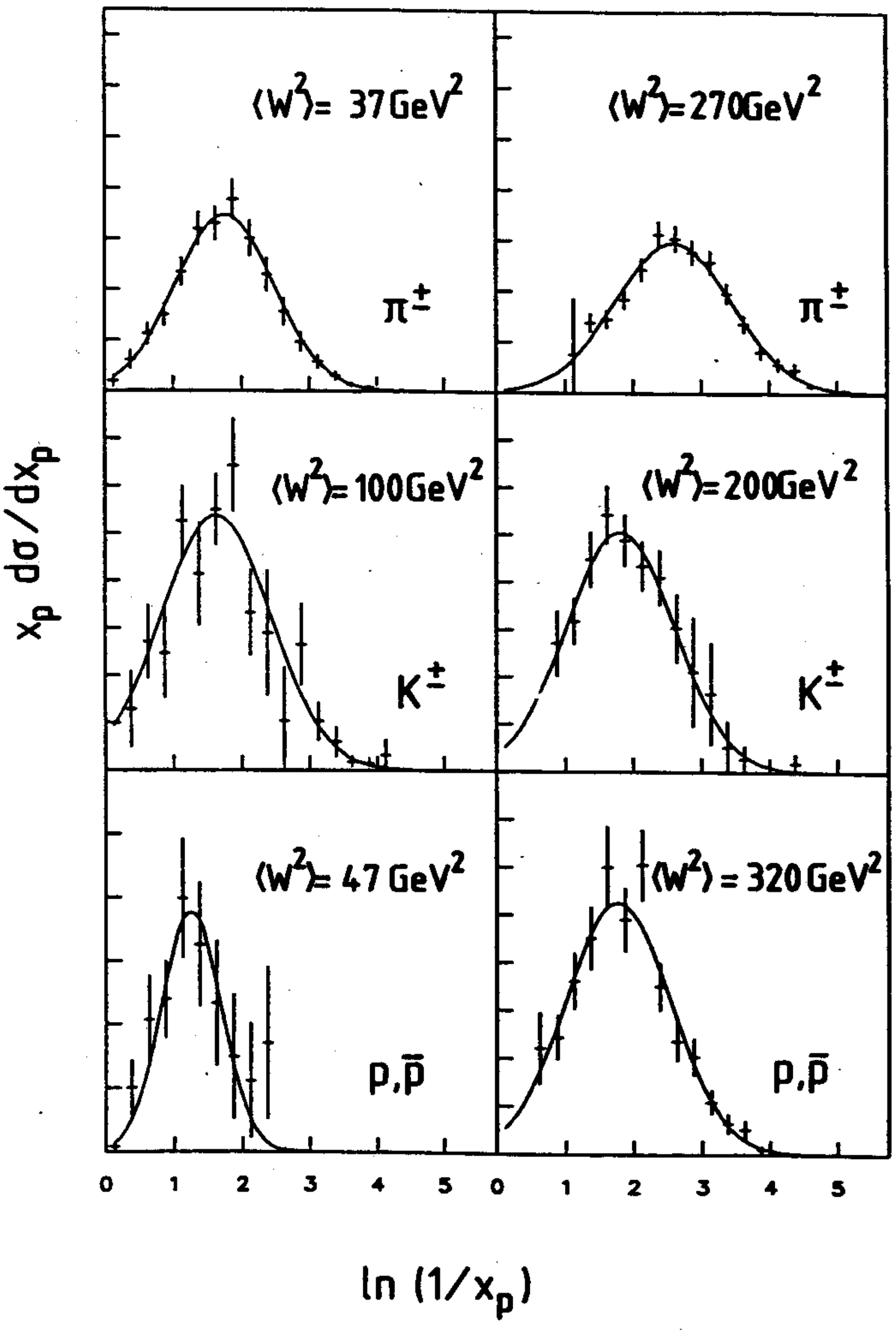
⟨W²⟩= 37GeV²
π±
⟨W²⟩=270GeV²
π±
⟨W²⟩=100GeV²
K±
⟨W²⟩=200GeV²
K±
⟨W²⟩= 47 GeV²
p,p̄
⟨W²⟩ = 320 GeV²
p,p̄
x_p dσ/dx_p
0
1
2
3
4
5
0
1
2
3
4
5
ln (1/x_p)

FIG. 23

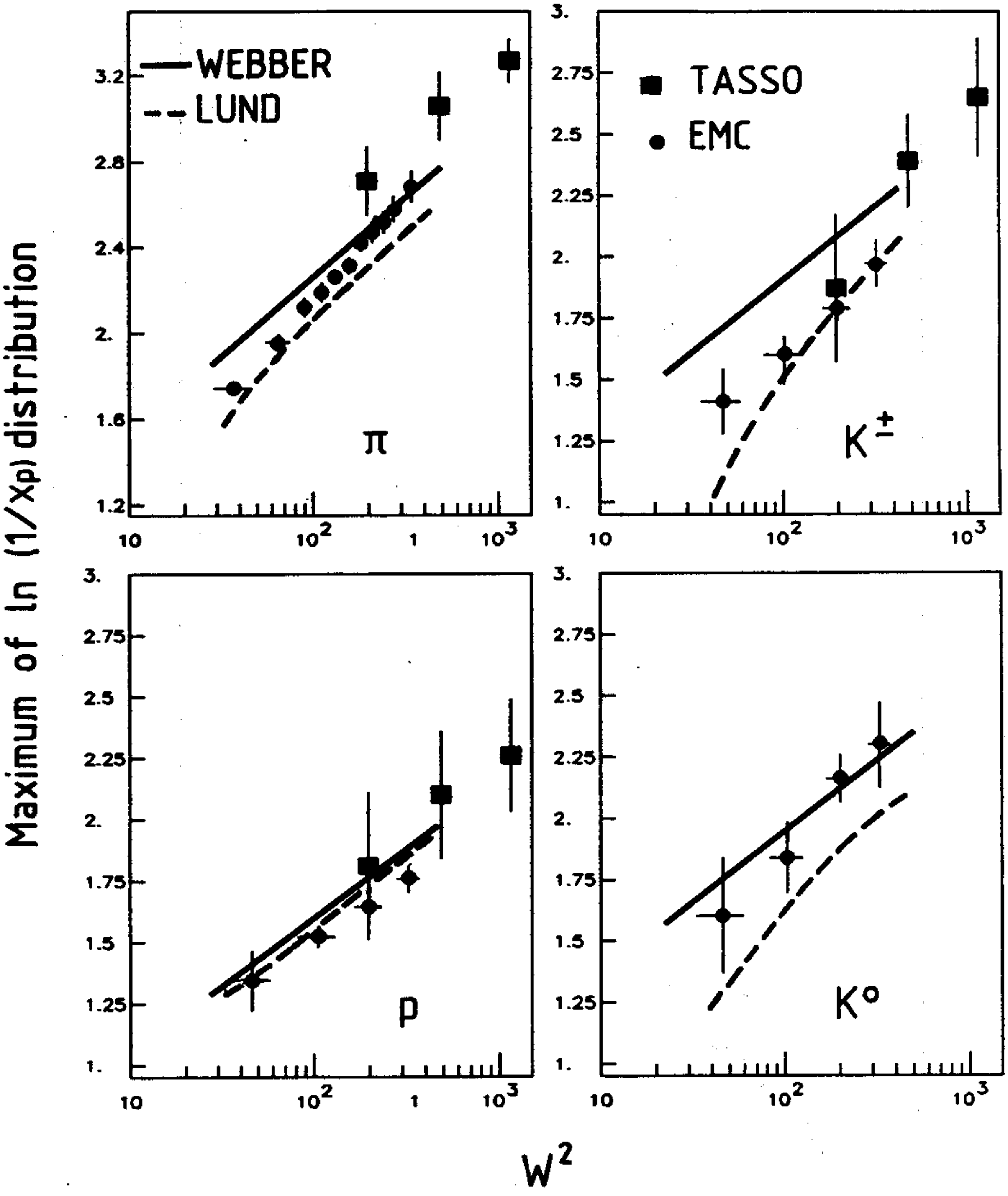

WEBBER
LUND
TASSO
EMC
Maximum of ln (1/Xp) distribution
W²
π
K±
p
K°
3.2
2.8
2.4
2.
1.6
1.2
3.
2.75
2.5
2.25
2.
1.75
1.5
1.25
1.
10
10²
1
10³

FIG. 24

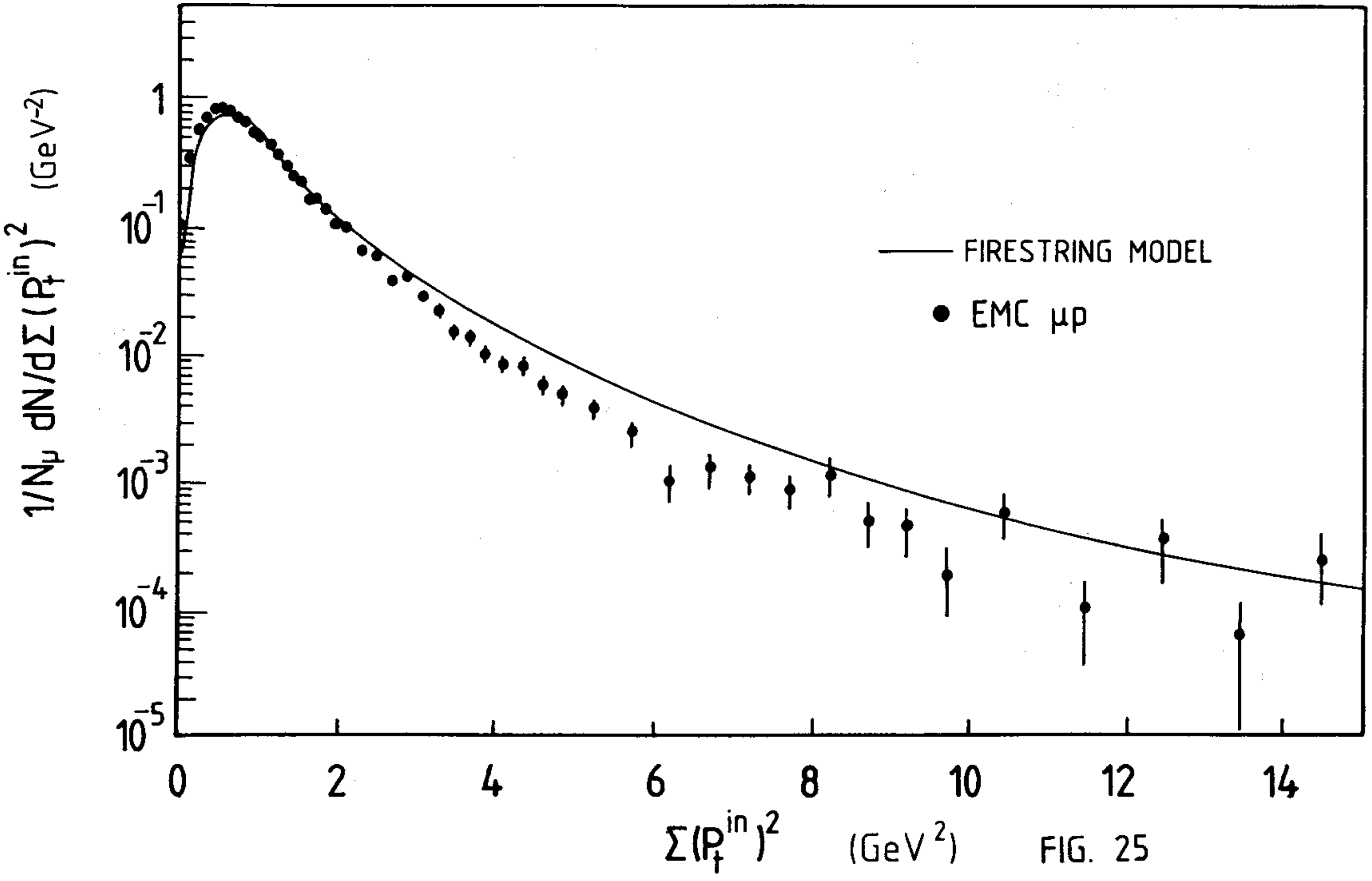
1/N_μ dN/dΣ(P_t^in)^2 (GeV^-2)
1
10^-1
10^-2
10^-3
10^-4
10^-5
0
2
4
6
8
10
12
14
Σ(P_t^in)^2 (GeV^2)
FIRESTRING MODEL
● EMC μp

FIG. 25

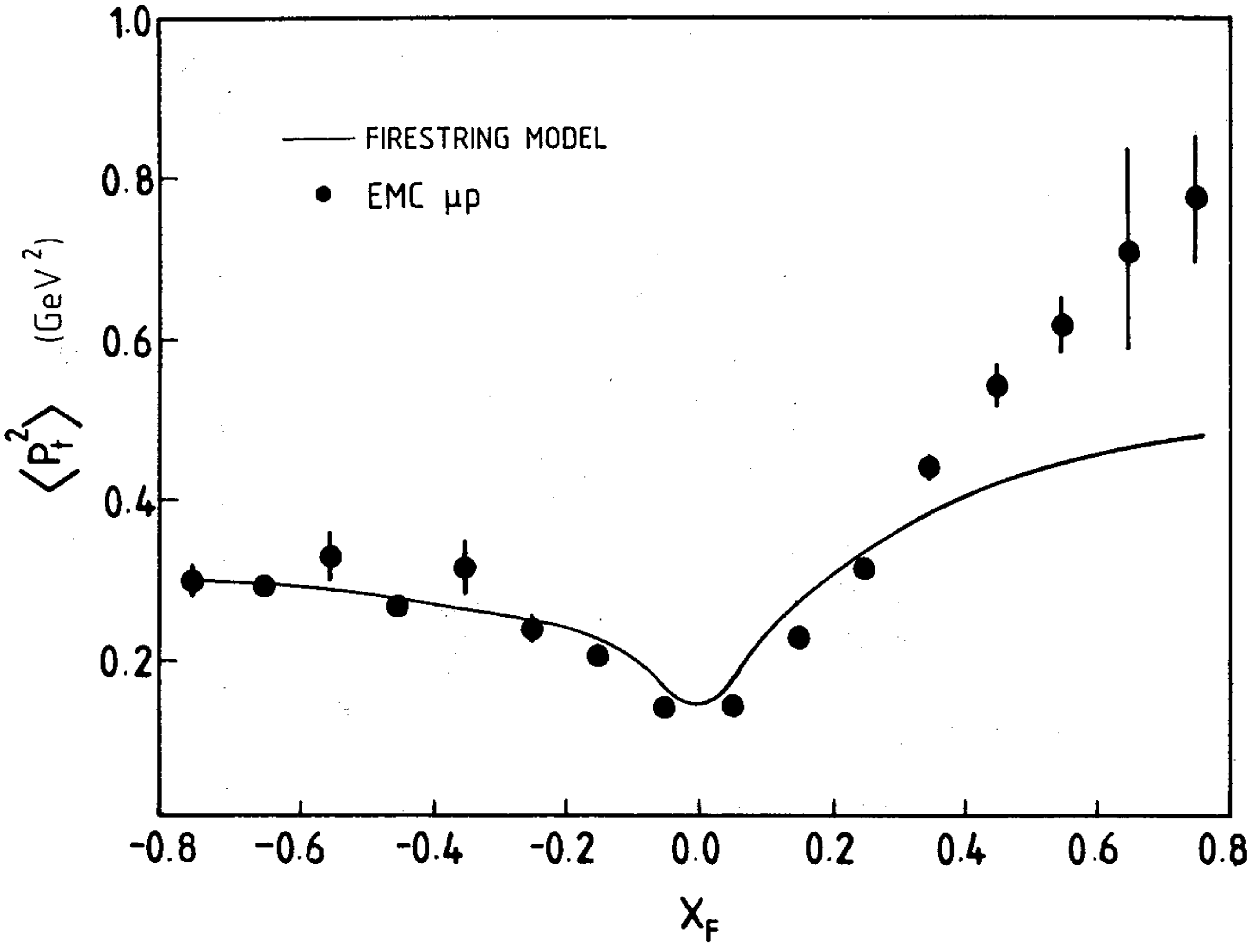
FIRESTRING MODEL
EMC μp
$\langle P_t^2 \rangle$ (GeV^2)
1.0
0.8
0.6
0.4
0.2
-0.8
-0.6
-0.4
-0.2
0.0
0.2
0.4
0.6
0.8
X_F

FIG. 26

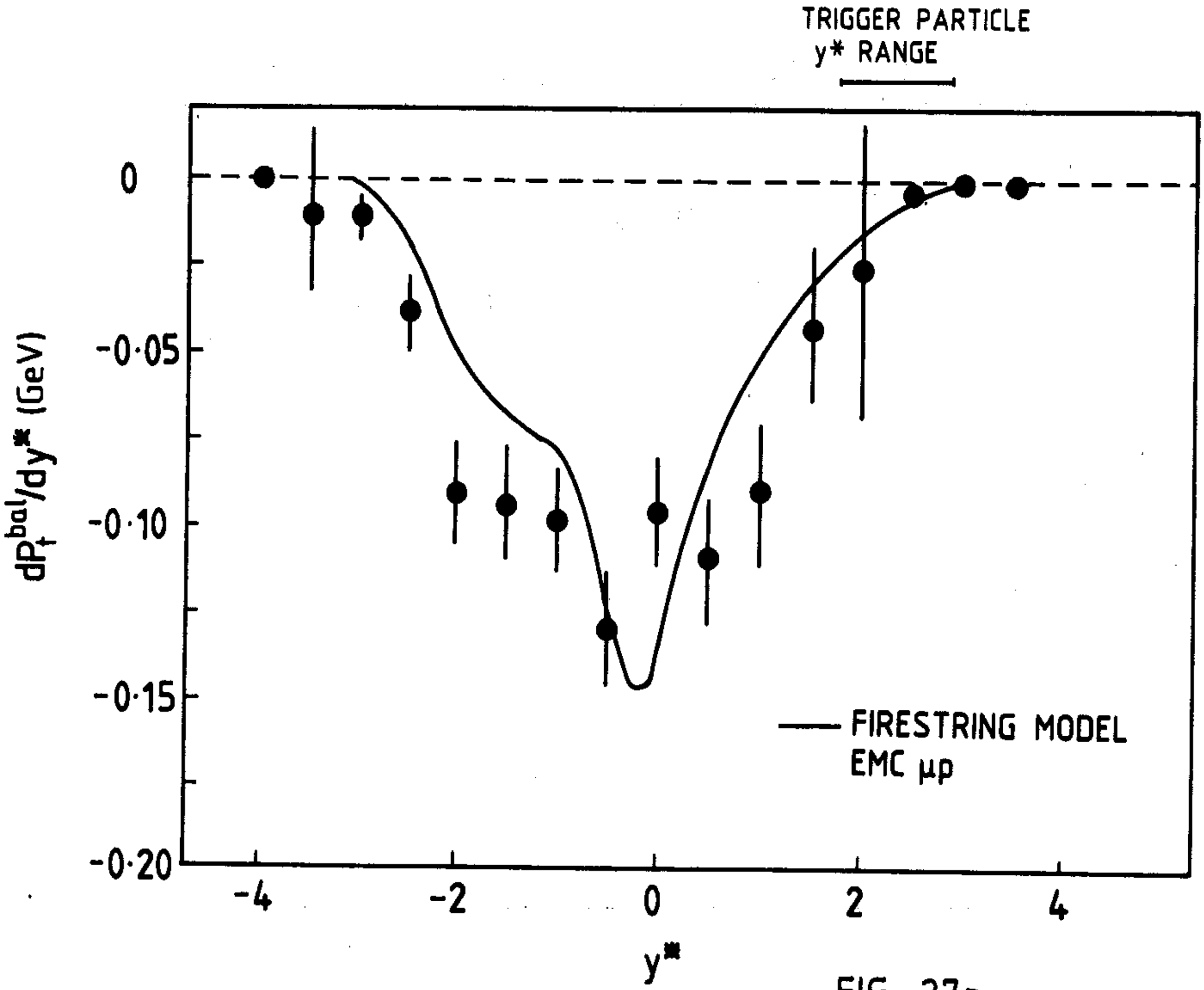
TRIGGER PARTICLE
y* RANGE
0
-0·05
-0·10
-0·15
-0·20
dP_t^{bal}/dy^* (GeV)
-4
-2
0
2
4
y*
FIRESTRING MODEL
EMC μp

FIG. 27a

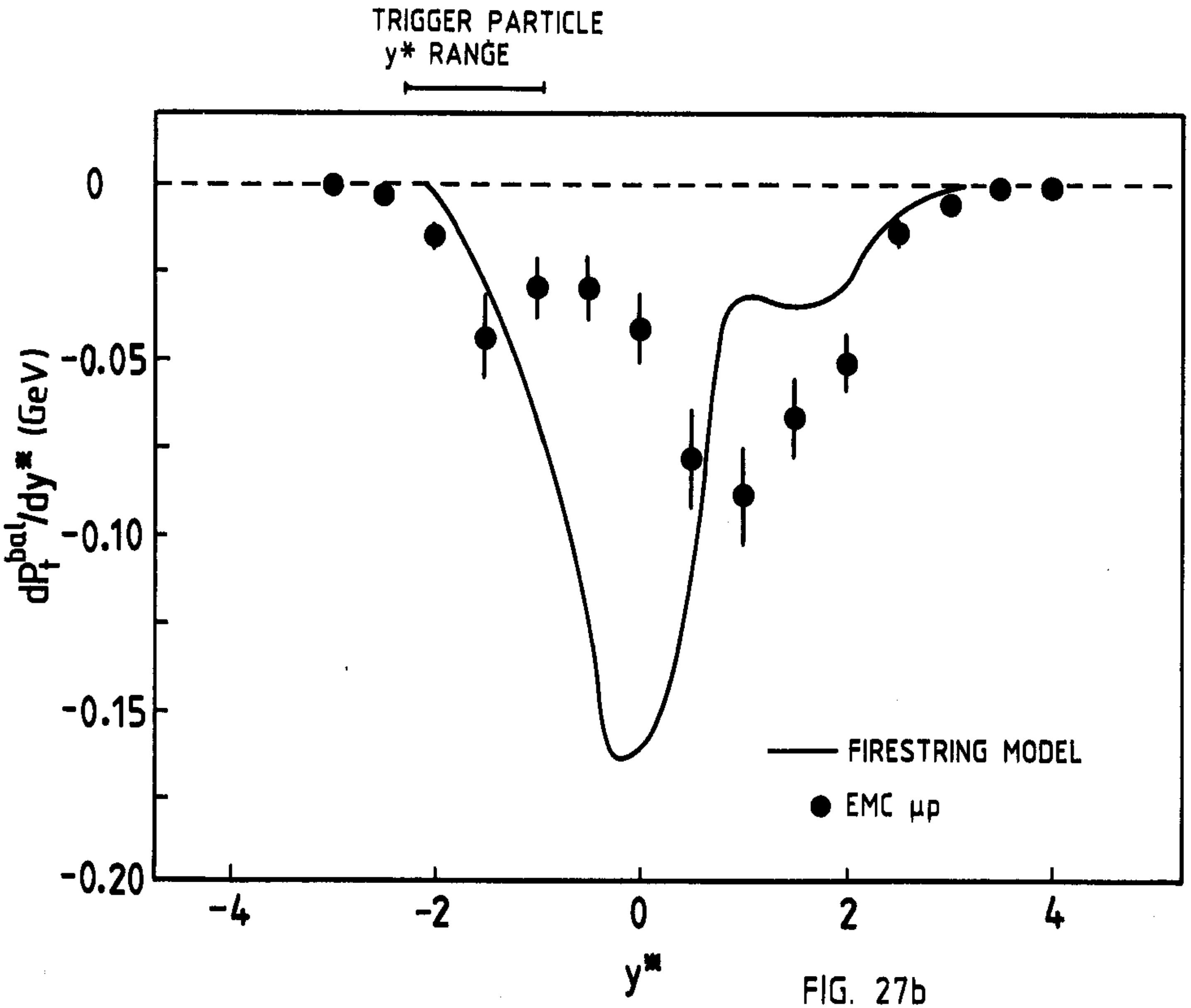
TRIGGER PARTICLE
y* RANGE
dP_t^{bal}/dy^* (GeV)
0
-0.05
-0.10
-0.15
-0.20
-4
-2
0
2
4
y*
FIRESTRING MODEL
EMC μp

FIG. 27b